Friction

Research Article

Advanced cavitation damage and erosion modeling for journal bearings in high-power density engines: Towards enhanced performance and reliability

Javier Blanco-Rodríguez[1,✉], David García-Rodiño[1], Martí Cortada-Garcia[2], Francisco José Profito[3], Jacobo Porteiro[1]

Cite this article: Blanco-Rodríguez J, García-Rodiño D, Cortada-Garcia M, et al. *Friction* 2026, **14**(7): 9441218. https://doi.org/10.26599/FRICT.2026.9441218

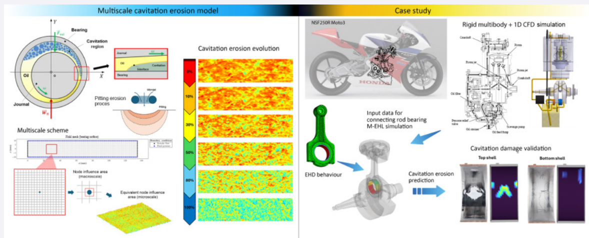

ABSTRACT: Reliability is critical in high-power density engines, where components operate under extreme conditions to achieve optimal performance. These demanding conditions give rise to complex multiphysics and multiscale interfacial phenomena, contributing to early wear stages, poor performance, and catastrophic engine failure due to severe mixed lubrication, cavitation damage, fatigue, and overheating effects. Therefore, enhancing the durability of such engines is paramount. This study investigates cavitation erosion in high-power density engines, with a particular focus on the connecting rod journal bearing. A novel multiscale cavitation erosion (MCE) model is presented, integrated with a mixed-elastohydrodynamic lubrication simulation framework. Realistic boundary conditions for bearing load, oil supply hole position, and pressure are obtained from a multibody dynamic simulation analysis of the entire system. The proposed multiscale cavitation erosion model predicts the cavitation damage energy at each computational mesh node within the macroscopic bearing domain. This energy serves as a threshold to erode the corresponding microscale area surrounding the macroscale node region. The equivalent microscale area is then coupled with the bearing surface topography, and material removal is simulated using a novel cavitation erosion algorithm. The proposed model is applied to evaluate the evolution of cavitation damage in the connecting rod bearing of a motorsport engine. The analysis considers various influencing factors, including engine speed, bearing clearance, lubricant formulation, and oil temperature. The findings reveal key insights into the cavitation erosion mechanisms, highlighting the significant influence of lubricant formulation and engine speed on erosion severity in the studied bearing.

KEYWORDS: cavitation erosion; numerical modeling; motorsport; mixed elastohydrodynamic lubrication (M-EHL); ultralow viscosity; lubricants

1 Introduction

The constant pursuit of performance improvements is a defining characteristic of high-tech engineering systems. Original equipment manufacturers (OEMs) continuously strive to optimize performance and maintain a competitive edge. In this context, motorsports demand cutting-edge technological advancements toward efficiency and durability [1, 2], while sustainability has become an increasingly critical factor [3]. Consequently, engineers must balance the need for high performance with the durability required to meet operational constraints. The scenario that any competitor wants to avoid is a mechanical failure due to reliability issues [4].

High-power-density internal combustion engines (ICEs) are highly complex systems with multiple interacting subsystems. To gain a competitive advantage, high-performance engines are often designed to operate at higher rotational speeds, thereby maximizing power output while maintaining consistent torque delivery [5]. This strategy is particularly relevant for naturally aspirated ICEs, where power output is primarily governed by engine speed.

However, operating at such high rotational speeds, often exceeding 16,000 revolutions per minute (r/min), introduces significant challenges that compromise engine lifetime. Increased inertial loads from centrifugal forces and orbital dynamics at rotational clearance joints, such as journal bearings, intensify tribological interactions [5, 6]. These inertial forces can surpass combustion loads at the connecting rod at elevated speeds,

[1] CINTECX, Universidade de Vigo, Grupo de Tecnoloxía Enerxética (GTE), Lagoas-Marcosende s/n, Vigo 36310, Spain. [2] Repsol SA, Madrid 28045, Spain. [3] Department of Mechanical Engineering, Polytechnic School of the University of São Paulo, São Paulo 05508-220, Brazil.

✉ Corresponding author. E-mail: Javier.blanco.rodriguez@uvigo.gal

Received: April 20, 2025; Revised: December 30, 2025; Accepted: January 26, 2026

© The Author(s) 2026. This is an open access article under the terms of the Creative Commons Attribution 4.0 International License (CC BY 4.0, http://creativecommons.org/licenses/by/4.0/).

increasing lubrication severity. In parallel, journal bearings can also experience highly transient lubrication conditions, leading to rapid fluctuations in oil film thickness. Such fluctuations can induce severe cavitation erosion when low-pressure regions within the lubricant film transition abruptly to high-pressure zones due to journal orbital movement [7].

Cavitation-induced damage in lubricated contacts has been investigated over the past few decades [8–13], with researchers distinguishing between different cavitation mechanisms. Engine oils, known for their significant solubility of gases/air, can contain dissolved gases and air entrainment levels of up to 15% by volume [14]. Due to the molecular structure of hydrocarbon-based lubricants, fluid film cavitation occurs in distinct manners. In gaseous cavitation, dissolved gases separate from the oil when pressure drops slightly below atmospheric levels. In contrast, vapor cavitation occurs only at lower pressures due to the lubricant's inherently low vapor pressure [15, 16]. The distinction between these cavitation mechanisms in lubricated contacts is well-established in Refs. [17, 18]. However, the energy released during gaseous and vapor cavitation differs considerably, directly influencing the severity of surface erosion [19–21].

Highly dynamic lubrication conditions induce oil vapor cavitation, leading to abrupt localized energy release, the primary cause of surface erosion generated by the vapor bubble implosions and shock waves [8, 15]. While several studies have examined the energy balance in cavitation processes [17, 22–24], a consolidated approach for quantifying this energy remains elusive due to various uncertainties. Key challenges include convection and conduction heat transfer, bubble–wall interactions during the collapse, phase change heat release, erosion intensity influenced by flow velocity, and localized variations in fluid temperature. The highly transient nature of cavitation, along with its strong dependence on operating conditions and fluid properties, further complicates the development of reliable mathematical models and experimental validations. Consequently, establishing a standardized predictive approach for cavitation-induced damage remains a significant challenge.

This research presents a novel model for cavitation damage and surface erosion, based on an energy-based approach, to quantify material removal. The proposed framework aims to support high-power-density engine manufacturers and lubricant companies addressing erosion damage issues in sliding bearing systems, particularly in connecting rod bearings. The model provides insights into the critical operating conditions and lubricant properties that influence cavitation damage, including rotational speed limits, bearing clearance, surface coatings, engine configuration, oil temperature, saturation pressure, viscosity, and density.

The structure of this paper is as follows. The first part presents the proposed cavitation damage model, detailing the cavitation energy and the multiscale cavitation erosion (MCE) calculations. The second part applies the model to a case study, evaluating the impact of cavitation damage evolution on high-power density engines under real-world operating conditions.

2 Models and methods

2.1 General equations in mixed elastohydrodynamic lubrication (M-EHL) simulation

This section provides an overview of the mathematical modeling used to simulate the M-EHL behavior of the journal bearing investigated in this work. However, to condense this presentation, we will not delve into specific details, as the primary focus of this contribution is the development of an MCE model, which addresses the complex interactions between lubrication and cavitation erosion phenomena. For a comprehensive understanding of the mathematical formulations and underlying principles employed in similar contexts, please refer to Refs. [25, 26]. Figure 1 illustrates the scheme used for the M-EHL model.

The modified isothermal steady-state Reynolds equation describes lubricant fluid flow at the journal bearing interface, complemented by the Elrod–Adams p–θ mass-conserving cavitation algorithm for managing cavitation dynamics. The lubricant film thickness is described using local coordinates, while the effects of elastohydrodynamic (EHD) deformation are modeled through a reduced finite element approach to ascertain surface displacements. The rheological properties of the lubricant are calculated through temperature, pressure, and shear rate dependencies, utilizing the Barus equation for viscosity–pressure relationships and the Carreau–Yasuda model for shear-thinning behaviours. The Greenwood and Tripp model is employed to calculate microscale asperity contact pressures. The load balance and the frictional forces due to fluid and solid interactions are calculated to ensure equilibrium under various loading conditions. For further information on the mathematical aspects and validation of the adopted M-EHL simulation model, the reader is referred to Refs. [25–30].

2.2 Cavitation damage energy

This section presents the multiscale cavitation damage model based on an energetic approach, which quantifies the amount of energy transferred to the surface due to oil vapor bubbles. A brief explanation of background concepts is necessary to describe this phenomenon adequately. Therefore, the methods and equations used for this model are mentioned below.

2.2.1 Vapor bubble dynamics

Several authors have studied the vapor bubble dynamics in a fluid flow, with the most notable contribution recognized to the Rayleigh–Plesset [10, 31, 32] in cavitation dynamics. The generalized Rayleigh–Plesset [24] equation is derived for liquid flows with zero velocity slip between the fluid and bubbles, and it considers bubble growth and collapse based on the two-phase continuity equations for the liquid, vapor, and their mixture. Figure 2 shows the different stages of a vapor bubble during cavitation, divided into nucleation, growth, maximum size, and

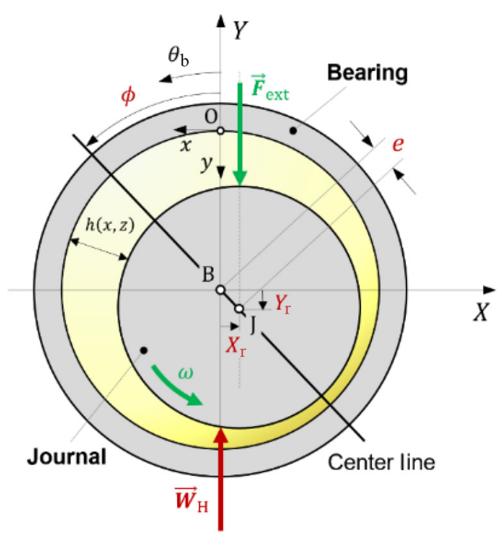

Fig. 1 Journal bearing scheme.

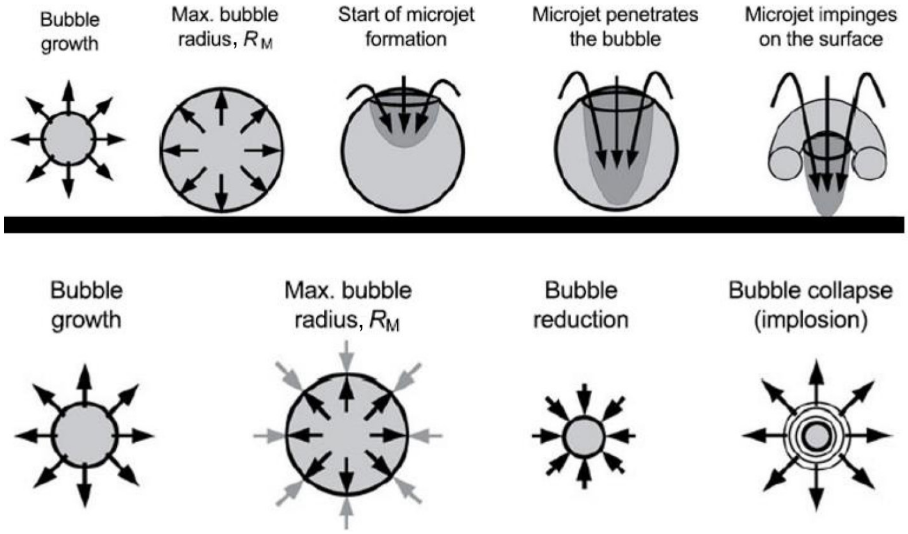

Fig. 2 Bubble collapse stages. (Top) bubble collapse near a wall and (bottom) bubble collapse in a free flow [33].

collapse. It can also be observed that the collapse method depends on how close the bubble is to a wall.

However, in this study, the bubble growth is assumed to reach its maximum size in equilibrium before collapse. Therefore, a balance between aerodynamic drag and tension forces can be used to obtain a correlation for the bubble's maximum radius. This simplification is carried out due to the limitation of the fluid domain definition, where the fluid is not discretized in the radial direction of the journal bearing. This scenario is defined as a homogeneous cavitation discretization, which establishes the same vapor fraction for all the fluid in the radial direction. The maximum radius reached on these conditions is defined in Eq. (1), where "r_b" is the bubble radius, "W_e" is the Weber number for bubbles, "σ" is the liquid surface tension, "ρ_{liq}" is the liquid density and "v_{brel}" is the relative velocity of the bubbles from the wall, which is about significantly smaller than the liquid velocity as mentioned in Ref. [31]. In this study, "v_{rel}" is 10% of the liquid velocity based on the assumptions provided in Ref. [34], which established a specific slipping ratio of the vapor bubbles immersed in the liquid flow.

$$r_b = 0.0305 \frac{W_e \sigma}{\rho_{liq} v_{rel}^2} \tag{1}$$

Equation (1) uses the Weber dimensionless number, which describes the relationship between inertial and surface tension forces. It is commonly used to assess critical conditions in fluid dynamics scenarios, such as the formation, breakup, and stability of fluid droplets and bubbles. In this case, the study is focused on bubble dynamics, where Weber number can be distinguished in the following ranges [35]: breakup ($W_e > 10$), formation and growth ($W_e < 1$), and oscillation ($1 < W_e < 10$). Therefore, as this study presents a highly dynamic scenario, W_e is calculated locally for each mesh node depending on its field working conditions.

$$W_e = \frac{\rho_{liq} v_{rel}^2 h}{\sigma} \tag{2}$$

where h is film thickness of fluid.

Regarding the time duration of the cavitation event, the M-EHL simulation predicts time frames that cannot distinguish cavitation bubble collapse due to its short duration. To address these different timescales, the Rayleigh bubble collapse time [31, 32] is used as the reference duration to calculate the average energy rate released per vapor bubble. This time represents the duration of a vapor bubble from its stabilization at maximum radius until collapse due to pressure differences, as shown in Eq. (3). The bubble's destabilization causes the collapse event due to the variation in surrounding liquid pressure when it reaches its maximum size.

$$t_c = 0.915 r_b \sqrt{\frac{\rho_{liq}}{p_{liq} - p_{sat}}} \tag{3}$$

where t_c is the collapse time and p_{sat} is the saturation pressure.

2.2.2 Vapor bubbles distribution

Regarding the bubble location in the discretization space, the problem is defined on a 2D mesh where the radial direction is unidimensional. Therefore, the bubbles can be described as a function of the vapor fraction in terms of bubble density per unit volume cell. Figure 3 illustrates a random distribution of vapor bubbles inside a cell, where the bubble density per volume can be calculated using Eq. (4).

$$\eta_b = \frac{1-\theta}{\theta} \frac{1}{4/3\pi r_b^3} \tag{4}$$

In Eq. (4), θ is the fluid fraction from the Elrod–Adams p–θ mass-conserving cavitation algorithm and r_b is the vapor bubble radius.

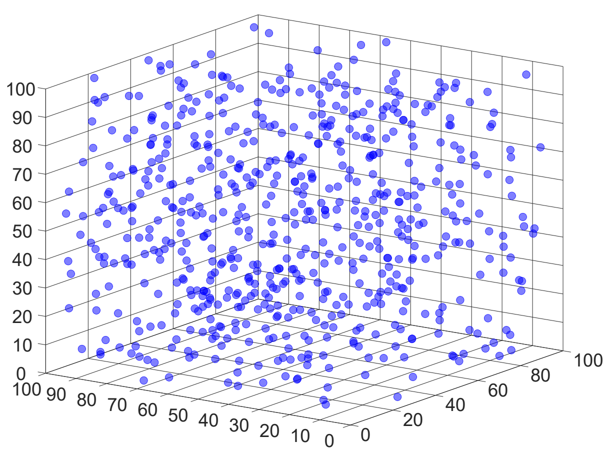

Fig. 3 Random distribution of vapor bubbles in a cell.

清華大学出版社 Tsinghua University Press | SciOpen

Regarding the physical behavior of vapor formation in fluid flows, several authors distinguish between small vapor bubbles and large bubbles or vapor clouds based on the void fraction. This differentiation is crucial when addressing the damage caused by bubble implosions and shock waves, particularly in terms of the bubble density and its location. In Fig. 4, a correlation method is proposed to determine the bubble density as a function of void fraction, which is the inverse of the fluid fraction used to obtain the bubble density, and it considers only the oil vapor produced by cavitation. The authors propose this correlation based on Ref. [36], but it should be noted that it is not a validated correlation and highly depends on the specific case study and its boundary conditions. In this study, a correction factor f_{bv} is presented to account for the probability of bubble implosion and shock waves as a function of bubble size, which is directly correlated with the void fraction (Fig. 4). This correction factor is applied multiplicatively to the bubble density within a given volume cell to derive the effective bubble density that reflects the probability of implosion and shock wave.

Bubble formation in a free flow tends to localize vapor formation in the low-pressure regions of the diverging sections. This scenario is common in sliding bearings due to orbital movement and hydrodynamic effect. Similar scenarios are found in hydrofoils and diverging test channel sections, as mentioned in Ref. [37], which supports this proposal. The approach of this work is to model this uneven vapor distribution in the radial direction across the oil film thickness. In this way, homogeneous cavitation discretization is solved without modeling a full three-dimensional (3D) domain simulation.

Regarding the modeling technique for the vapor distribution, several sources are taken from Refs. [18, 38, 39] to create a template vapor distribution function. Consequently, a probability density function (PDF) for oil vapor is employed, characterized as a function of the dimensionless oil film thickness, which serves as a local reference for each node, specifically for this bubble distribution function. This PDF reaches its peak probability in proximity to the steady surface, where the low-pressure region is located, indicating a higher probability of oil vapor presence in this critical area. This function is not validated experimentally but is based on experimental Refs. [38, 39]. Where the vapor distribution is not uniform across the oil film thickness, a specific test of this dynamic scenario can be used in future research to validate the function. This paper presents this function as a novel implementation in cavitation damage modeling, depicted in Fig. 6.

The density function gives a distribution ϕ of the vapor bubbles across the film thickness in the radial direction, but there must be an established limit above which the bubbles' implosions and shock waves cannot cause damage to the surface. Therefore, to address this dependence, a threshold value is used in the vapor bubbles distribution function to count only the bubbles that cause damage to the surface. This threshold is based on the relative wall distance γ (ratio between bubble radius and the oil film thickness), which is fixed at 1.5 based on the literature values [40, 41].

To determine the local h_{lim} threshold at each designated node, the bubble radius calculated at that specific node is multiplied by the relative wall distance γ to derive the corresponding threshold for that node. Subsequently, to estimate the cumulative probability value of the bubbles associated with the derived h_{lim}, this value must be normalized by the local oil film thickness. This normalization yields the threshold value in the dimensionless oil film thickness scale, which quantifies the presence of bubbles that may contribute to surface damage based on the probability distribution shown in Fig. 6. This factor is used in Eq. (5) to obtain the number of bubbles that cause damage.

$$h_{\mathrm{lim}} = \gamma \cdot r_{\mathrm{b}} \tag{5}$$

To account for the total energy accumulated by the vapor bubbles, it is necessary to calculate their total mass at a specific instant before the collapse. Consequently, the internal energy associated with the phase change and temperature differential can be calculated. Equation (6) represents the vapor mass associated with a single bubble.

$$m_{\mathrm{b}} = \frac{4\pi}{3} r_{\mathrm{b}}^{3} \rho_{\mathrm{vap}} \tag{6}$$

where m_{b} is the mass associated to a single vapor bubble and ρ_{vap} is the density of oil vapor.

By the outlined methodology, the number of bubbles within a volume cell is determined as a function of the critical film thickness threshold, the surface area of the cell within the computational mesh, the bubble density depending on the void fraction, and the cumulative distribution function (CDF) characterized by the specified threshold distance. Consequently, the bubble density within a given cell, denoted as η_{b}, is rectified by two distinct factors. These factors account for the bubble distribution as a function of the void fraction, represented as f_{bv}, as well as the proximity to the bearing surface, designated as $\phi(h_{\mathrm{lim}})$. This correction ensures a refined approximation of the bubble dynamics about the underlying physical conditions.

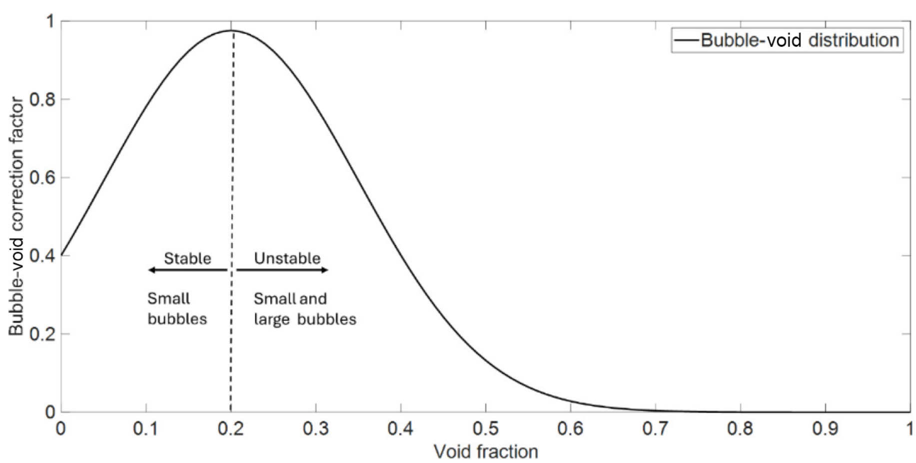

Fig. 4 Bubble–void fraction correction factor distribution.

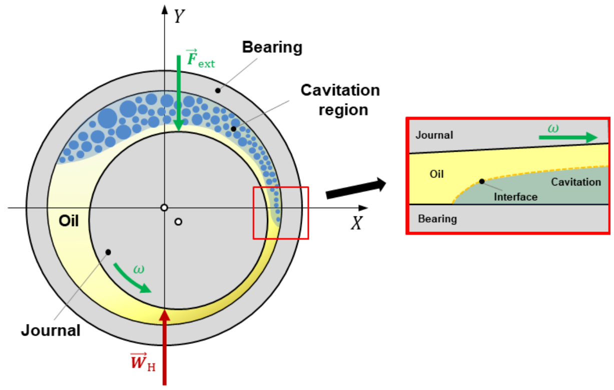

Fig. 5 Cavitation region distribution across oil film thickness in a journal bearing.

$$N_{\mathrm{b}} = h_{\mathrm{lim}} \cdot A_{\mathrm{node}} \cdot \phi\left(h_{\mathrm{lim}}\right) \cdot f_{\mathrm{bv}} \cdot \eta_{\mathrm{b}} \tag{7}$$

where A_{node} is the relative area to a node.

The total mass of vapor bubbles $m_{\mathrm{t\text{-}b}}$ is obtained with Eq. (8):

$$m_{\mathrm{t\text{-}b}} = N_{\mathrm{b}} \cdot m_{\mathrm{b}} \tag{8}$$

2.2.3 Vapor bubbles energy

Cavitation bubbles are generated through a phase change from liquid oil; therefore, their internal energy primarily arises from the latent heat of this process. However, as the pressure change is high compared to the surrounding fluid, considerable work is done during the bubble implosion due to the pressure difference. Additionally, this process is not thermally isolated, which allows heat conduction to occur in the surrounding fluid. The energy accumulated in the vapor bubbles results in a sudden change back to liquid, causing shockwaves and microjets. The intensity of the damage caused by this phenomenon depends on the distance to the surface, as addressed in numerous studies [17, 22, 42]. As the distance increases, the intensity of damage decreases drastically until the vapor bubbles travel freely and collapse without causing any harm to the surface. This consideration involves the threshold distance to the wall, which selects only the relevant vapor volume based on the CDF bubble distribution.

To assess the damage caused to the engine by cavitation, two primary terms are considered: the energy resulting from the pressure differential between vapor bubbles and the surrounding liquid, denoted as $E_{\Delta P}$, and the heat transfer and phase change of the vapor bubbles, referred to as E_{Q}. This assumption is supported by Refs. [22, 40, 43], where authors identify these terms as key contributors to cavitation damage, as presented in Eq. (9). Regarding the heat transfer from the vapor bubbles to the surrounding liquid, based on Plesset's assumption [10], it is estimated that the temperature drops by less than 1 °C due to the presence of vapor bubbles in the liquid. Therefore, this term is initially neglected but will be examined in detail in future studies.

$$E_{\mathrm{cav}} = E_{\Delta P} + E_{\mathrm{Q}} = \frac{4}{3}\pi r_{\mathrm{b}}^{3} \Delta p + m_{\mathrm{t\text{-}b}}\left(C_{\mathrm{e}} \Delta T + C_{\mathrm{L}}\right) \tag{9}$$

where E_{cav} is the cavitation energy in the vapor bubbles.

Regarding the pressure impact correlation, there is an intrinsic dependence on the distance of the bubble from the wall. As mentioned in Ref. , the maximum intensity of the impact pressure is identified at 0.75 of γ. Below and over that distance, the intensity is drastically reduced. The farther distance is identified as the threshold h_{lim}, previously used to identify the potentially damaging bubbles across the film thickness.

2.2.4 Cavitation wear load

The damage model presented in this study focuses on addressing local wear due to cavitation erosion. For this purpose, a new variable is defined to account for the cavitation wear power per area on each node of the hydrodynamic mesh. This variable is named cavitation wear load $\overline{W}_{\mathrm{cav}}$, which will be used as the average erosion power per revolution or combustion cycle. The power is obtained by dividing the cavitation energy by the Rayleigh bubble collapse time. This relation is proposed as a direct physical correlation due to the duration of the collapse event, which is the accumulated energy. $\overline{W}_{\mathrm{cav}}$ is proposed as a macroscale magnitude to quantify the average damage produced by cavitation in a node area of influence in a certain period.

$$\begin{aligned} \overline{W}_{\mathrm{cav}} &= \frac{1}{T}\int_{t}^{t+T} \frac{E_{\mathrm{cav}}}{A_{\mathrm{node}} t_{\mathrm{c}}} \mathrm{d}t \\ &= \frac{1}{T}\int_{t}^{t+T} \frac{\frac{4}{3}\pi r_{\mathrm{b}}^{3} \Delta p + m_{\mathrm{t\text{-}b}}\left(C_{\mathrm{e}} \Delta T + C_{\mathrm{L}}\right)}{A_{\mathrm{node}} 0.915 r_{\mathrm{b}} \sqrt{\dfrac{\rho_{\mathrm{liq}}}{p_{\mathrm{liq}}}}} \mathrm{d}t \end{aligned} \tag{10}$$

A set of boundary conditions is established to determine the correct cavitation energy released during the collapse event and

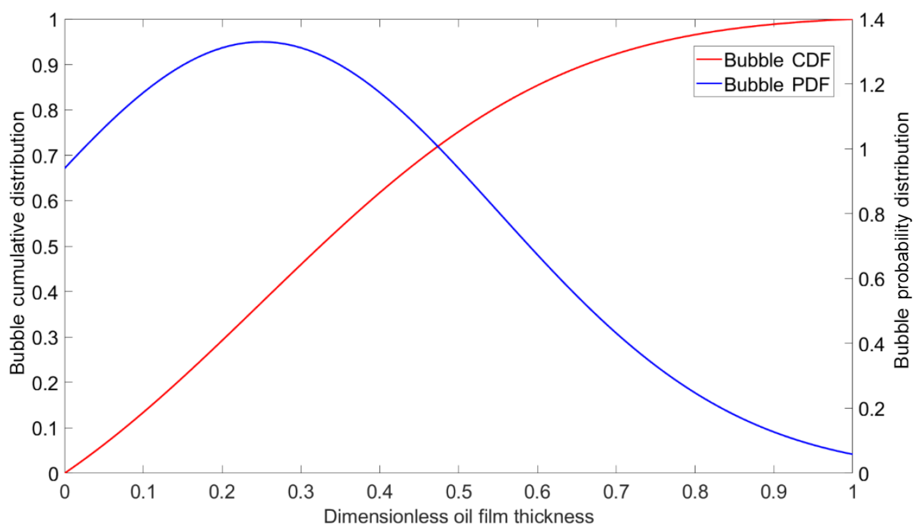

Fig. 6 Vapor bubble distribution function across the oil film thickness.

https://doi.org/10.26599/FRICT.2026.9441218

identify the collapsing events at the oil film thickness. These conditions are related to vapor fraction and bearing orbital movement. Therefore, the first condition establishes a positive vapor fraction in the previous timestep; the second condition sets a zero-vapor fraction in the current timestep; and the third condition only allows a positive gradient of oil film thickness, so the collapse must happen in the diverging region. These three conditions must be fulfilled to calculate the cavitation wear load.

2.2.5 Energy damage accumulation

As the period increases at certain working points with a critical value of cavitation wear load, damage accumulates in local regions of the bearing, corresponding to the collapse conditions. This damage accumulation can be determined with the cavitation wear load and the period of residence in those circumstances. However, this damage accumulation mechanism defines a new variable: the surface material fatigue resistance. Thus, cavitation implosions and shock waves must reach a certain energy level to cause surface damage. To address this condition, a correlation of the implosion impact pressure for cavitation events, as adopted in Ref. [44], is used as a variable to accumulate energy damage once the value of the impact pressure overcomes the yield strength of the bearing surface material.

As reported in Ref. [41], the maximum bubble impact pressure is 0.75γ. Therefore, this maximum impact pressure will be used as a conditional variable to accumulate energy damage on the surface only when its value exceeds the yield strength of the material surface. Equation (11) accounts for the accumulated average damage energy in the material over time. The time step is calculated using a constant increasing factor that doubles the previous time step, starting with 100 times the period at the specific rotational speed.

$$\overline{E}_{\mathrm{cav}}(t) = \overline{E}_{\mathrm{cav}}(t_0) + \overline{W}_{\mathrm{cav}}(t) \cdot t_{\mathrm{step}} \tag{11}$$

Regarding the damaging energy accumulated, the cavitation events are counted along the engine cycle by the number of vapor bubbles near the bearing surface at each node. The distance of these bubbles to the surface must be below the threshold limit established for bubbles to potentially cause damage, defined as h_{lim}. This condition is based on the yield strength limit, which counts these events as damage implosion due to the assumption of elastic behavior of the material below the yield strength. The maximum pressure impact is calculated with Eq. (12) based on Ref. [45], which is directly evaluated against the yield strength of the bearing to accumulate cavitation damage energy when the yield strength is overcome.

$$P_{\mathrm{impact}} \simeq 2.76c\sqrt{\rho P_{\mathrm{collapse}}} \tag{12}$$

where P_{impact} is maximum pressure impact, c is speed of sound, ρ is the fluid density, and P_{collapse} is the bubble collapse pressure.

The summation of these cavitation events throughout the engine cycle is utilized in the erosion process when the accumulated cavitation energy exceeds the energy necessary to cause cavitation erosion at the mesh node, which is characteristic of each material.

A nonlocal standard function is applied to enhance the time-averaged field results of the impact pressure and cavitation wear load, which shows a mesh dependency issue due to the spatial discretization of the hydrodynamic mesh. This issue was expected, as cavitation occurs locally and requires a high level of detail to capture all the transient changes. A nonlocal solution provides a smooth transition between changes in field values, avoiding local overshoots.

2.3 Cavitation erosion

Once the accumulated damage energy related to cavitation is determined, the following step is to correlate the amount of material that can be removed from the surface due to cavitation erosion. The authors propose a novel multiscale approach to quantify the material eroded by the cavitation phenomenon, wherein the micro-geometry is modified locally in terms of accumulated damage energy. Hence, macro-geometry is fed with relevant statistical variables in local coordinates based on the microscale variation. This approach enables the determination of changes in contact and lubrication boundary conditions in local coordinates at the macroscale.

2.3.1 Pit spherical cap equation

Cavitation damage is typically associated with surface damage known as pitting, which is characterized by microcavities formed in the damaged material due to the implosion of vapor bubbles. The geometry of these pits is not standardized and regular, as it depends on various boundary conditions. Therefore, a general definition is used for this study based on the proposal in Ref. [42]. This definition assumes the pitting geometry to be a spherical cap, as it is typically a shallow indentation on the surface material with a larger radius than depth.

The intrinsic relationship between the spherical cap geometrical parameters is shown in Eq. (13), where R is the spherical cap radius, h is the pitting depth, and D is the pitting diameter.

$$R = \frac{(D/2)^2 + h^2}{2 \cdot h} \tag{13}$$

To characterize the shape of pits, it is necessary to establish a relationship between the depth and diameter of the pit. A relationship between resilience strain caused by cavitation damage $\varepsilon_{\mathrm{cav}}$ and the ratio of pitting depth h and the pitting diameter D, shown in Eq. (14). This is an approximate correlation based on experimentation of many samples and fluids, as mentioned in Ref. [42].

$$\varepsilon_{\mathrm{cav}} \simeq 0.8 \cdot \frac{h}{D} \tag{14}$$

With these two equations, the resulting pitting depth h and pitting diameter D can be obtained for a given spherical cap radius R.

The cavitation mean strain in the cavitation impact with the surface is a variable that depends on the material properties and the severity of the bubble collapse. Journal bearings typically

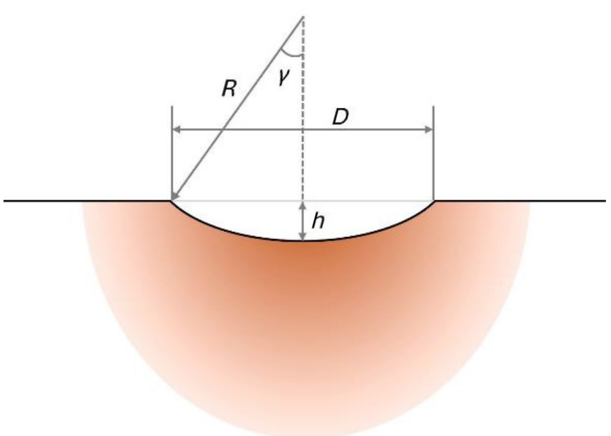

Fig. 7 Pit spherical cap scheme.

feature a soft coating or elastic material on their surface, thereby increasing the cavitation mean strain compared to other materials. As surface material in bearings is not usually characterized to obtain a realistic stress-strain curve, constant cavitation mean strain will be used, following the results reported in Ref. [42], where data on the mean strain obtained in experimental tests of cavitation erosion are presented for three different materials (AL7075, stainless steel, and Nickel aluminium bronze alloy), which yielded mean values between 15% and 25%. Therefore, the cavitation mean strain selected will be around this range, considering the specific materials used in the case study. As a note for this assumption, following Hook's law shown in Eq. (15) would lead to unrealistic values of cavitation mean strain because this law is correlated with elastic behaviour, while bearing overlay materials behave in the plastic regime due to their low yield strength.

$$\varepsilon = \frac{\mathrm{UR}}{E} \tag{15}$$

where "UR" is the ultimate resilience obtained from Eq. (15) and "E" is the elastic modulus.

$$\mathrm{UR} = \frac{\mathrm{UTS}^2}{2 \cdot E} \tag{16}$$

In Eq. (16), "UTS" is the ultimate tensile strength. This equation enables the calculation of resilience strain, relating this material property to the cavitation erosion model.

It is important to mention that cavitation erosion does not follow the same material properties correlations as tribological wear with hardness, as mentioned in Ref. [7]. Instead, cavitation damage in overlay bearing materials is better correlated with the ultimate resilience because this magnitude accounts for the strain energy to failure or the ability to sustain repeated strain without cracking. However, this correlation does not work in any material, as mentioned in Ref. [7], showing discrepancies. A direct correlation between cavitation erosion and bearing overlay material properties has not been established in the literature; therefore, this topic should be investigated further to enhance erosion prediction.

This cavitation erosion model proposed a new formulation for predicting the spherical cap radius, which will be used to define the pitting geometry based on the previous equations. Therefore, as previously described in Section 3.2, the damage energy accumulated per area caused by repeated cavitation implosions in the surface material is used to predict the pitting geometry. The number of pits on the surface is strictly related to the number of bubbles located below the threshold damage h_{lim}. These pits are located randomly within the damaged area. Equation (17) shows the spherical cap radius prediction based on accumulated damage energy. This equation establishes a threshold damage energy per node that must be accumulated to initiate the erosion process. This energy to failure per area, EF, is calculated based on the ultimate resilience, UR and the material coating thickness t_{coating}, which is shown in Eq. (17).

$$R = R_\infty - \frac{R_\infty - R_0}{\left(1 + \frac{\bar{E}_{\mathrm{cav}}}{\mathrm{EF}}\right)^{k_{\mathrm{cav}}}} = R_\infty - \frac{R_\infty - R_0}{\left(1 + \frac{\bar{E}_{\mathrm{cav}}}{\mathrm{UR} \cdot t_{\mathrm{coating}}}\right)^{k_{\mathrm{cav}}}} \tag{17}$$

where R_0 is the minimum spherical cap radius, which is equal to the vapor bubble maximum radius, R_∞ is the maximum spherical cap radius of a pit, k_{cav} is the cavitation intensity index defined in Eq. (18), $\bar{E}_{\mathrm{cav}}$ is the cavitation damage energy accumulated on a node, and EF is the characteristic energy to failure proper of the bearing shell material defined as $\mathrm{UR} \cdot t_{\mathrm{coating}}$.

$$k_{\mathrm{cav}} = \frac{U \cdot U^+}{C} = \frac{U^2}{C \cdot \sqrt{\frac{\tau_{\mathrm{w}}}{\rho}}} \tag{18}$$

where "U" is the relative velocity between journal and bearing, "U^+" is the dimensionless relative velocity, which is equal to $U^+ = U/\sqrt{\tau_{\mathrm{w}}/\rho}$, "$\tau_{\mathrm{w}}$" is the oil film shear stress, "ρ" is the oil density, and "C" is the speed of sound in the oil. This cavitation intensity index is a parameter similar to Archard's wear intensity constant, which is adjusted based on experimental data. However, this cavitation damage index only depends on the calculated variables in the fluid, and it is intended to emphasize the cavitation damage dependency within the flow velocity, which several authors have concluded in Refs. [23, 46] as a main damage factor. Therefore, the higher the flow velocity, the bigger the constant.

Figure 8 shows the evolution of the spherical cap radius within

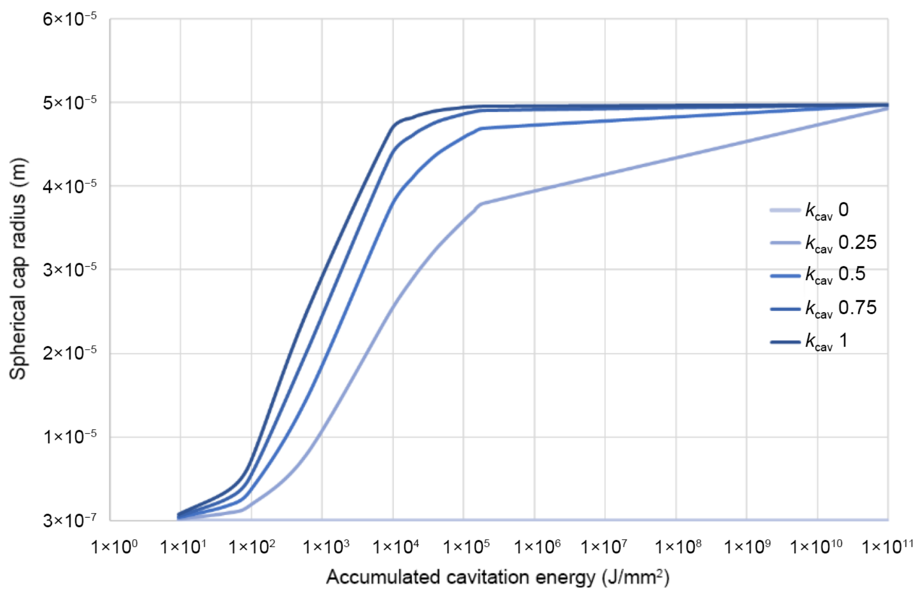

Fig. 8 Spherical cap evolution within accumulated cavitation energy and different cavitation intensity indexes.

accumulated cavitation energy and different cavitation intensity indexes, where 0 is the lowest intensity, and 1 is the maximum intensity. Therefore, the higher this index is, the faster the erosion in the bearing surface will occur.

2.3.2 Microscale surface erosion

To achieve a correlation between the different scales used in M-EHL simulations, a parameter must be identified that can be evaluated at both micro and macro scales. In this study, an energetic approach is employed, where the damage energy is calculated on the macro scale, considering critical scenarios for cavitation erosion. The damage energy accumulated in each node of the bearing surface at the macroscale serves as a damage counter to initiate the cavitation erosion process. Once the accumulated cavitation energy per node reaches the energy to fail the material, material removal due to cavitation erosion begins. The pit geometry is based on the definition of a pit spherical cap at the microscale equivalent area of each node, and the spherical cap calculation is based on the initial energy required for the material to fail. As the erosion process is likely to occur in the same place several times, the material removal is proportional to the number of times it is eroded. A scheme of cavitation erosion evolution is shown in Fig. 9, where the various stages of erosion are depicted in the pitting region. In this figure, a bubble implosion is displayed during the collapse event, creating a microjet that will severely impact the bearing surface. Some authors [40, 45] proposed correlations for microjet velocity for water in controlled environments that reported a speed of 150 m/s when impacting the wall.

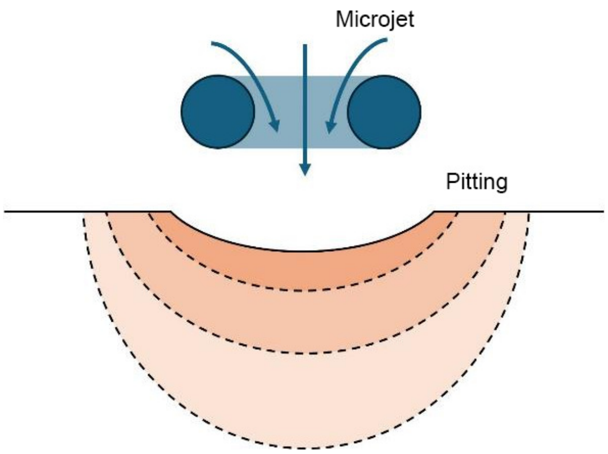

Fig. 9 Cavitation pit erosion evolution scheme.

However, the cumulative collapse of bubbles in close regions can cause pitting propagation, which forms a bigger eroded region of similar characteristics. The pitting propagation is modeled through a novel erosion algorithm. The morphology of the pit is increased by repeated cavitation events following the spherical cap dimensions, which increases the diameter and depth of the pit in incremental stages as a function of accumulated cavitation energy. The propagation of the pit with neighboring pits is carried out according to the proximity condition, which unifies the eroded regions into a single one when the pits are close enough. Once the pits are closed in a region, the growth of this region is uniform in all directions, as cavitation events occur in the eroded area. A simplified scheme of the erosion evolution processes with these topological operations is illustrated in Fig. 10, where initial pits start to grow from left to right and from top to bottom. When the pits are close enough, the eroded area unifies and expands in all directions until it becomes a single pit, as shown in the bottom proper illustration.

This erosion process is carried out in a topography that is equivalent in area to a node of the hydrodynamic mesh on the macroscale. This topography represents the characteristics of the microscale, and it evolves within the cavitation erosion process. Figure 11 is one of the roughness samples from a journal bearing used in the cavitation erosion process. The region highlighted in black is presented in Fig. 11 as a detailed view of the different stages of the erosion evolution. The spatial discretization of this sample is 0.8 μm in both the X and Y directions and a total dimension of 1.4 mm in the X direction and 1.8 mm in the Y direction.

In Fig. 12, a real showcase of the cavitation erosion algorithm's performance is depicted at different stages of the cavitated area of the topography, ranging from 0% to 100%. It can be observed that in the initial stages of erosion, pits are mainly separated from one another. As the cavitated area increases, the pits become larger due to erosion propagation in the surrounding pits. A highly eroded surface is observed in the final stages, where small portions of material remain without erosion. When the surface is completely eroded, the topography resembles a new one with

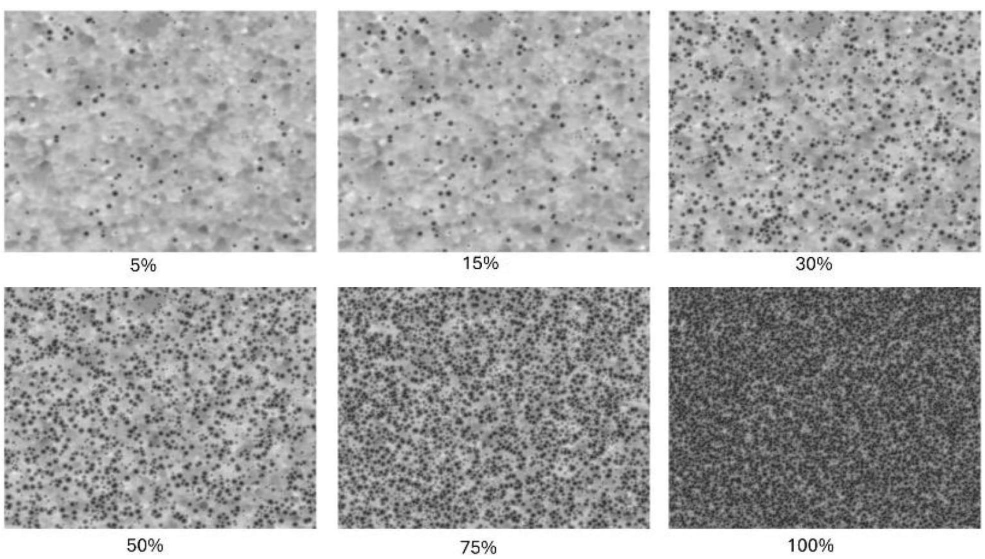

Fig. 10 Cavitation erosion propagation scheme.

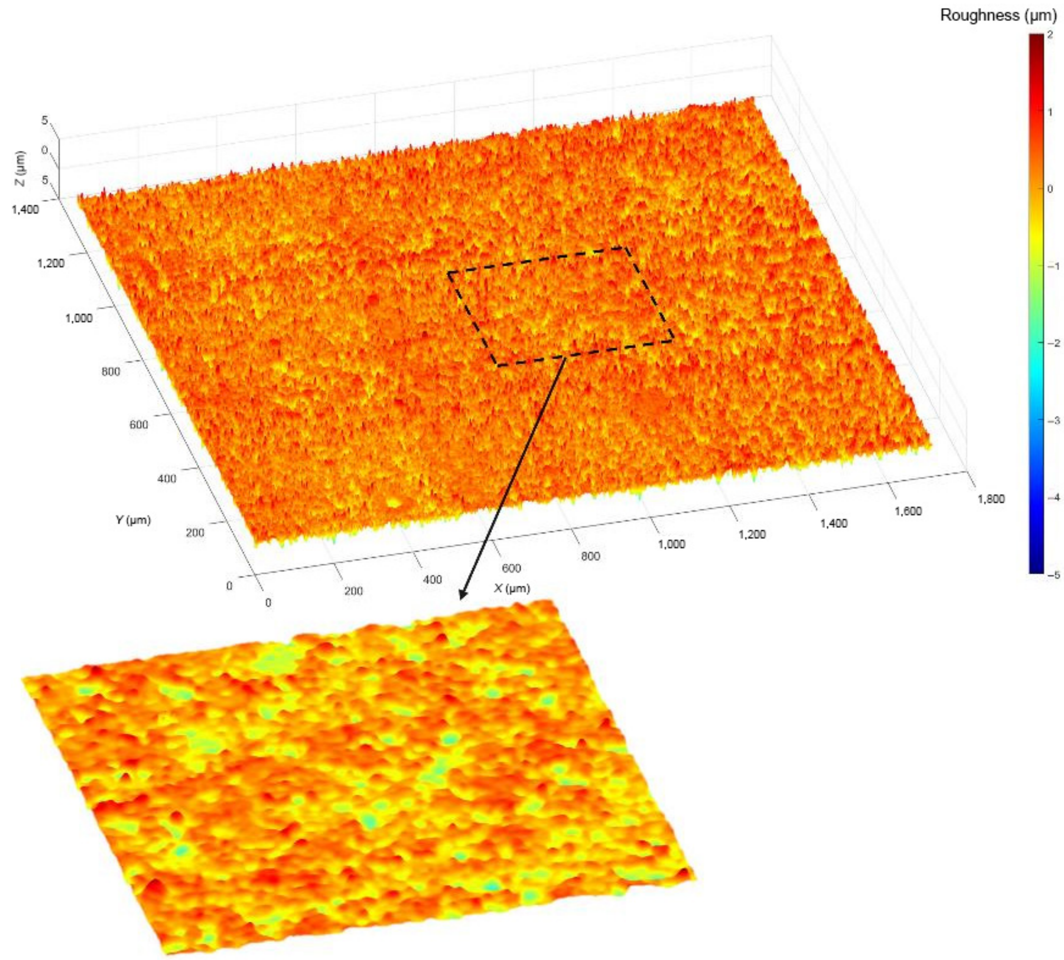

Fig. 11 Roughness sample used to analyze the cavitation erosion evolution.

different characteristics from the initial, and a mean plane with negative values results due to material removal.

This algorithm treats every hydrodynamic node at the macroscale as a single entity, so the erosion process differs from node to node, as the topographies are distinct. Additionally, the results from the M-EHL model used at each node are locally computed, so even slight differences in the oil film fraction will be noticeable.

2.3.3 Macroscale surface erosion

The correlation between the two solution scales in M-EHL simulation has several important points to consider: first, which general variables are meaningful from one scale to the other; second, how a local phenomenon in the microscale, such as cavitation, can disturb the M-EHL solution in the macroscale; third, which difference in scales is compatible to make a multiscale correlation.

Based on Refs. [47–49], it can be assumed that the microscale level has a notable impact on friction due to the surface roughness characteristics. This finding has been translated into several contact models to predict the tribological behaviour between surfaces. Another variable that may be significantly changed is the flow in thin oil films, due to the orientation of the asperities in the microscale.

Cavitation erosion has a significant impact on the surface roughness characteristics. After long periods or highly aggressive conditions, the surface overlay may fail due to fatigue caused by numerous vapor bubble implosions. This scenario can be found in many hydrofoils, pumps, or turbine applications. However, this study focuses on fluid film cavitation in sliding bearings, as observed in diesel or high-performance petrol ICEs subjected to highly dynamic conditions caused by load gradient changes or high engine rotational speed, respectively.

Regarding the scale difference, the multiscale correlation at the surface bearing is suitable for enhancing the understanding of small-scale phenomena that affect the typical working scale in lubrication studies. This correlation is carried out between variables calculated in millimeters with the M-EHL solver and computed in micrometers with the cavitation erosion routine. Surface characterization was conducted using the routine described in Ref. [50]. In Fig. 13, an illustration shows the differences between the two scales.

The variables computed in the microscale are the roughness parameters used in the Greenwood-Tripp equation and the wear depth in advanced erosion stages. With this novel dependency on cavitation erosion, a better assessment can be carried out for reliability and friction enhancement.

2.3.4 M-EHL and MCE models coupling

This section explains the comprehensive iterative algorithm framework and numerical solution methodology for the quasi-static elastic plain journal bearing system, integrated with an MCE model. The flowchart illustrated in Fig. 14 describes the routine steps implemented during the dynamic simulation. The steady-state solution of the M-EHL model is derived by resolving the nonlinear equilibrium equations governing the relative rigid body displacements of the journal, denoted as (X_r, Y_r), at each time step throughout the dynamic cycle.

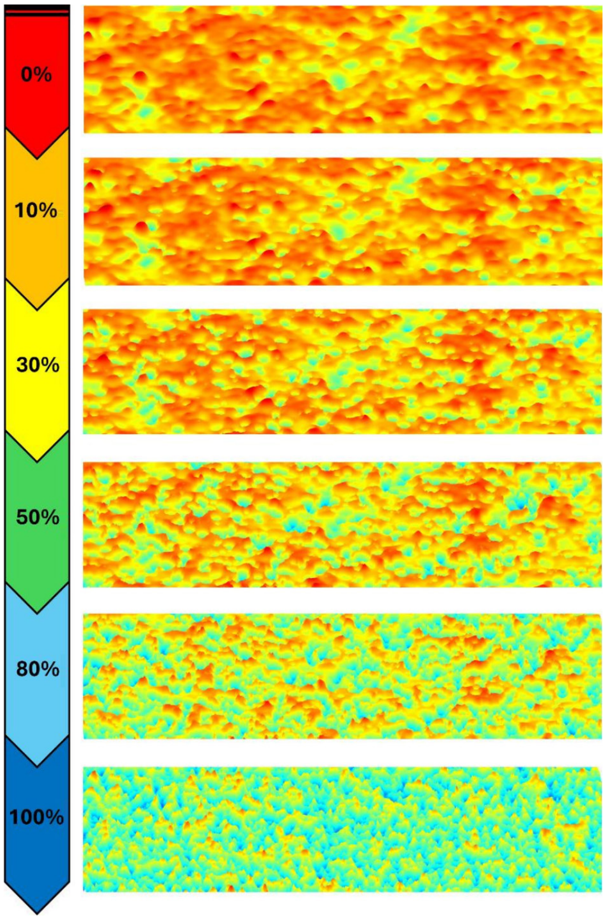

Fig. 12 Cavitation erosion stages.

To address these nonlinear equations and the EHL solution, the Newton–Raphson and point Gauss–Seidel method with Aitken acceleration (PGMA) algorithms are employed, utilizing Armijo's linear search technique to optimize the solution step size at each Newton–Raphson iteration. Within the framework of the Newton–Raphson iterative process, the Reynolds equation is numerically solved via the hybrid element-based finite volume method (EbFVM) as proposed by Profito et al. [27, 30], designed explicitly for lubrication problems encompassing mass-conserving cavitation on unstructured meshes.

Upon the completion of the dynamic cycle, the cavitation erosion algorithm calculates the corresponding macroscale variables, including cavitation wear load and the time step required to determine the cavitation energy at each node. Subsequently, the prediction of cavitation erosion is carried out through the application of the pit spherical cap equation and an erosion damage propagation algorithm, which evolves the surface topography at the microscale in each time step. After the surface erosion process, roughness parameters are computed. It is essential to note that modifications to surface roughness have significant implications for tribology and hydrodynamics. These changes can affect the coefficient of friction (CoF) in eroded regions and alter the average oil flow resulting from an increased gap between surfaces. Currently, these factors are not incorporated into the model. However, future developments of this code will integrate various parameters related to tribology and hydrodynamics, accounting for erosion and wear evolution. This integration will be implemented in each quasi-static solution loop of the EHL model to enhance the sensitivity of the proposed multiscale cavitation erosion model.

Following the execution of these subroutines, the subsequent variables within the macroscale M-EHL framework are updated to initiate the next iterative cycle: bearing geometry, roughness parameters, and operational conditions.

3 Case study: Cavitation damage prediction on high-power density engines

The case study selected is an engine mounted on a racing motorcycle from the Moto3 world championship. This

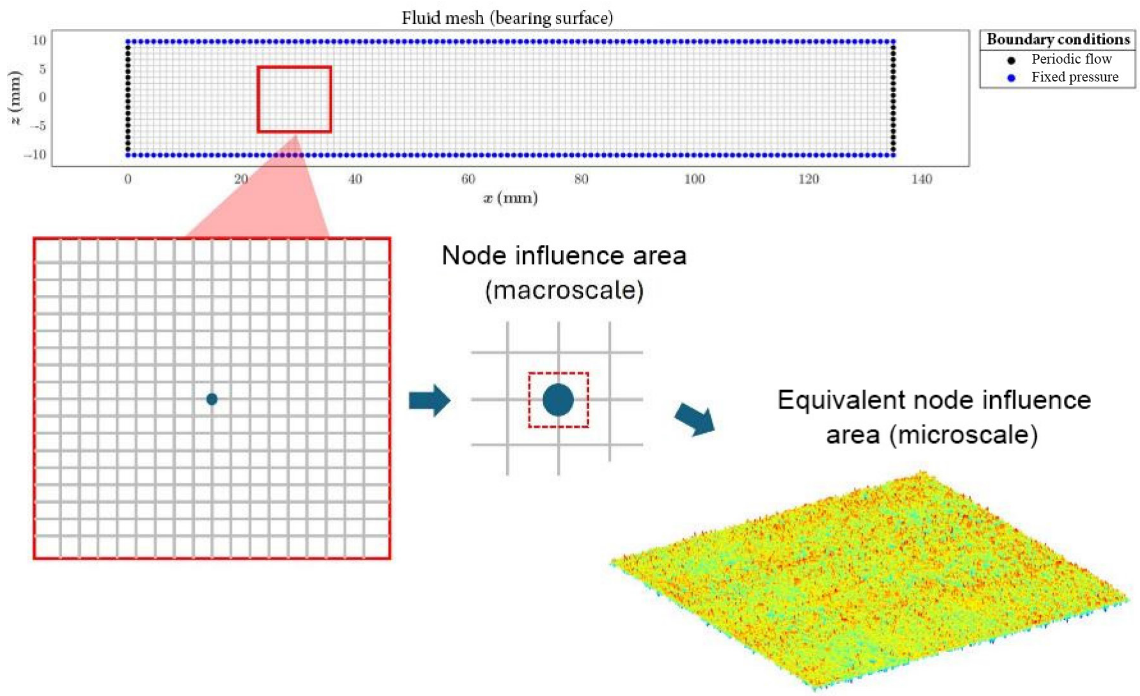

Fig. 13 Journal bearing multiscale scheme.

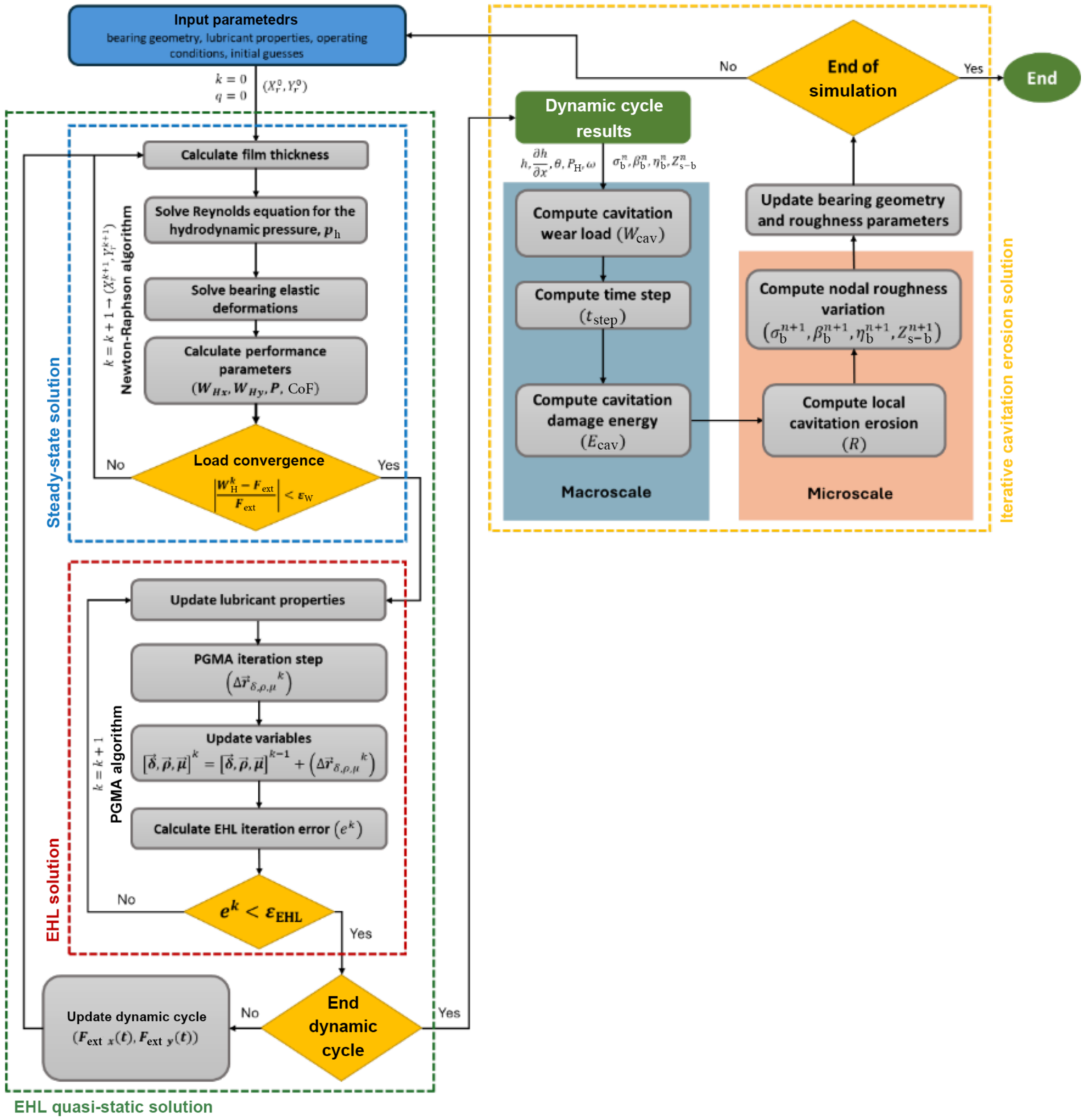

Fig. 14 Coupling scheme of M-EHL and cavitation erosion models.

powertrain operates under highly dynamic conditions where cavitation damage is found at the connecting rod bearings when high engine speeds are reached [5, 6]. A dynamic combustion cycle will be run in this specific case scenario with a constant average engine speed and oil temperature. This condition will be maintained for a specified period to address the evolution of cavitation erosion. A general scheme of the procedure carried out in this case study is shown in Fig. 15. General data is shown in Table 1 to enhance understanding of the selected vehicle.

3.1 Modeling strategy

This study uses two simulation models to predict cavitation erosion on the connecting rod journal bearing. First, a complete lubrication system model is developed, where a rigid multibody solution is used for the mechanical system, and a one-dimensional (1D) computational fluid dynamics (CFD) solution is used to obtain the lubricant behavior in the lubrication circuit, as modeled in other case studies [53]. This model generates the inputs for a detailed 3D M-EHL simulation of the connecting rod bearing, where dynamic variables from the lubrication system model include bearing load, crankpin supply holes position and pressure, journal and bearing rotational speeds.

3.1.1 Rigid multibody and 1D CFD simulation model

The lubrication system of the NSF250R is modeled to obtain the dynamic variables over the combustion cycle, which is then input into the standalone connecting rod bearing model. This simulation model was developed using GT-Suite commercial software. To achieve realistic behaviour, the oil feed pump is modelled in detail based on available data [51, 52], including variable volume chambers to represent rotor movement and a relief valve to control output pressure and flow. The lubrication circuit is modelled with oil galleries that pass through the oil filter and reach the bearings and piston jets. The oil returns to the sump, where it is picked up by the oil pump and retaken to galleries. To account for the dynamic loads of the engine

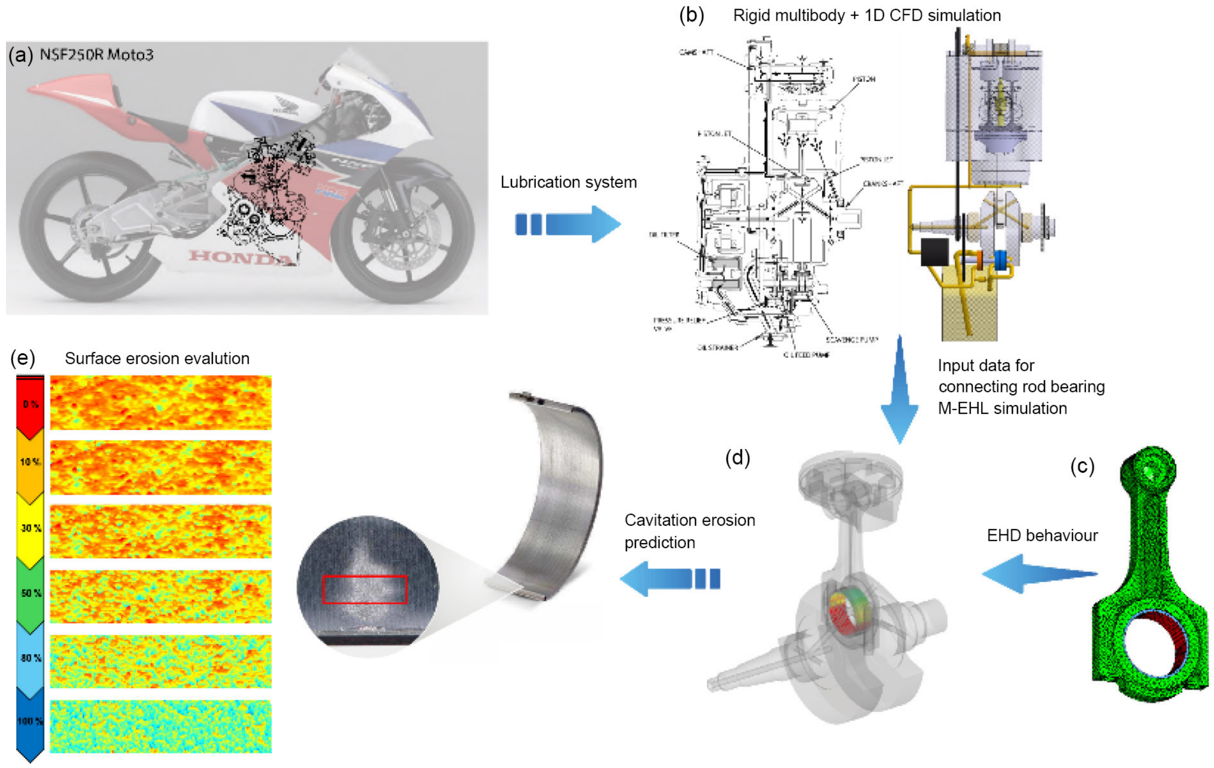

Fig. 15 Case study for cavitation erosion modeling: (a) NSF250R from Moto3, (b) lubrication system simulation model, (c) connecting rod FEM, (d) M-EHL simulation of connecting rod journal bearing, and (e) cavitation erosion simulation.

Table 1 General features of the NSF250R [51, 52]

Feature	Value
Model	NSF250R
Start of production	Year 2011
Number of gears	6, manual transmission
Model code	MR03
Kerb weight (kg)	84
Engine displacement (cc)	250
Engine configuration	Single cylinder, 4 stroke, liquid cooled
Bore × stroke (mm^2)	78 × 52.2
Lubrication system	Semi-dry sump
Compression ratio	12.3
Power/speed (kW/(r/min))	35.5/13,000
Torque/speed (N·m/(r/min))	28/10,500
Fuel	Petrol
Fuel injection system	PGM-FI
Engine intake	Naturally aspirated
Valvetrain	DOHC
Oil capacity (L)	1.27

assembly, the mechanical parts are modelled as a 1D mechanism to translate the load to the journal bearings. Combustion pressure is precomputed in a 1D combustion model and included in this model as lookup tables of combustion pressure as a function of the engine speed at different engine loads. Figure 16 shows a general scheme of the complete lubrication system simulation model.

This model aims to transfer realistic data to a standalone model, enabling a comprehensive study of cavitation erosion. Therefore, this model explanation is limited to a basic description that enables comprehension of the process for obtaining the input data for the connecting rod journal bearing. The instantaneous data gathered from this model include: X and Y loads at the journal bearing, supply pressure at the two crankpin holes, angular position of each supply hole, and rotational speeds of the crankpin and bearing.

3.1.2 M-EHL simulation model

The 3D M-EHL model aims to study local phenomena at the journal bearing, including tribological wear and cavitation erosion. As explained in the previous section, this simulation model was developed using academic software. The foundation of this detailed model is the finite element method (FEM) applied to the connecting rod bearing. This approach accounts for the elastic deformation of the structure due to the bearing load. The elastic deformation is influenced by both hydrodynamic and contact pressures, leading to the development of a fluid-structure interaction (FSI) model. The hydrodynamic (HD) mesh is adjusted to the bearing bounds and characteristics of the NSF250R, as the oil is fed by two moving holes at the crankpin, shown in Fig. 17. The spatial discretization of this mesh is included in Table 2.

The FEM developed for this simulation is depicted in Fig. 15(c), with a comprehensive description provided in Table 2. These parameters were obtained through an iterative analysis focused on achieving mesh independence in the simulation results. To optimize runtime efficiency, a combination of element types is employed, leveraging the reduction technique known as condensed FEM [54]. In this methodology, C3D8 elements are integrated into a stiffness matrix alongside CQUAD4 elements, which serve as the interface between the bearing and fluid domains. As a result, only the CQUAD4 elements are subjected to loading within the simulation, incorporating both mass and stiffness characteristics to account for the complete array of elements associated with the bearing. This strategy facilitates substantial improvements in computational runtime efficiency.

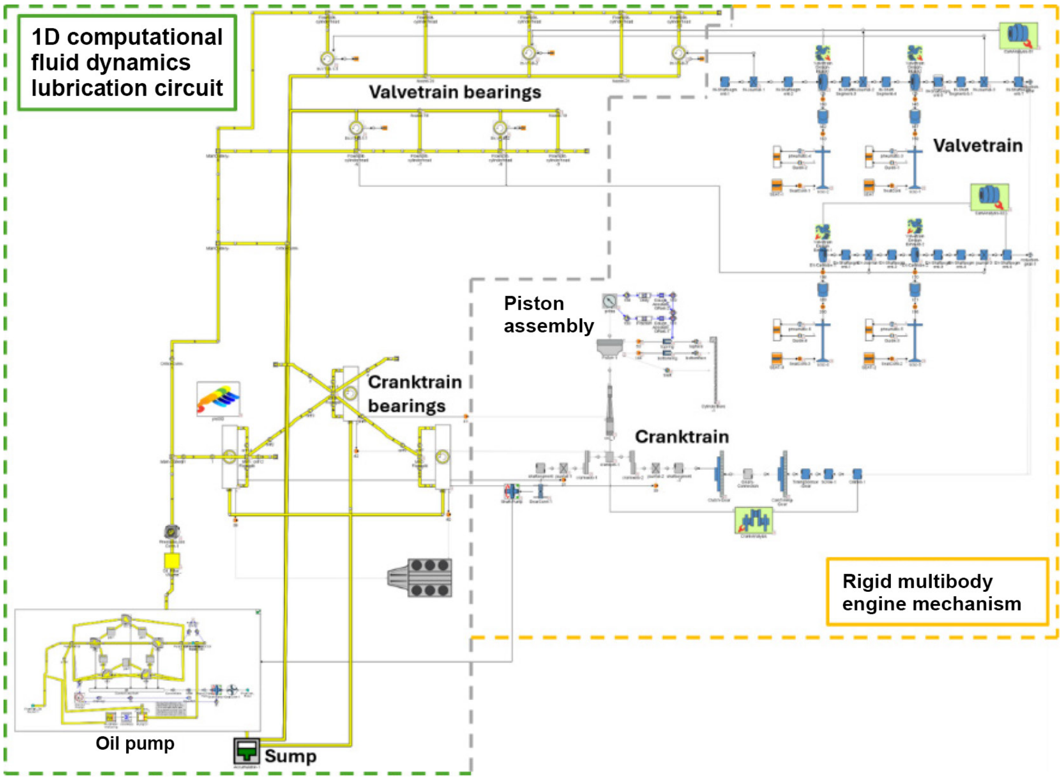

Fig. 16 Lubrication system simulation model.

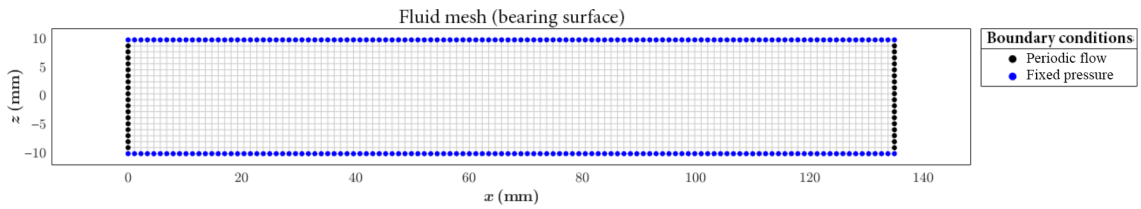

Fig. 17 Hydrodynamic mesh used in M-EHL simulation.

Table 2 Hydrodynamic and FEM mesh specifications

	Bearing HD mesh	Connecting rod FEM
Elements	2,384	35,200
Average size (mm)	1	1.33
Type of elements	CQUAD[2]	C3D8[1], CQUAD[2]
Nodes	2,550	15,150

[1] 8-nodes fully integrated linear solid element; [2] 4-nodes plate element.

Table 3 Repsol lubricant composition (%)

Component	Oil A	Oil B	Oil C
Group-V base stock [59]	80	47	50
Group-IV base stock [59]	19	40	40
Thickener	1	13	10

Table 4 Repsol lubricant properties

T_{ref}, 100 °C	Oil A	Oil B	Oil C
Density (kg/m³)	790.2	798.5	803.3
Kinematic viscosity (cSt)	6.30	8.02	12.1
Barus coefficient (1/bar)	1.1×10^{-3}	1.01×10^{-3}	1.01×10^{-3}
Oil dynamic viscosity (C_p) at 10 s^{-1}	4.94	6.37	9.62
Oil dynamic viscosity (C_p) at 10^{6} s^{-1}	4.92	4.28	4.94
CoF at mixed regime	0.063	0.069	0.060

3.2 Lubricant candidates

This study evaluates the wear characteristics of ultralow viscosity lubricant formulations, specifically Oil A, Oil B, and Oil C. Each formulation combines synthetic base stocks with a carefully selected array of additives, including viscosity modifiers, friction modifiers, antioxidants, corrosion inhibitors, detergents, anti-wear agents, anti-foam additives, nanoparticles, and dispersants, as in Refs. [55–58]. Table 3 details the compositional breakdown, highlighting that the synthetic base stock constitutes the majority of the mass percentage of each formulation, with additives integrated in equivalent proportions across oils. The lubricants were formulated and characterized at the Repsol Technology Lab in Mostoles, Madrid, Spain.

Table 4 presents the properties of lubricant formulations evaluated for wear protection at 100 °C, revealing significant differences among them. Oil A is characterized by Newtonian behavior, with constant dynamic viscosity across shear rates, while Oils B and C display shear-thinning behavior consistent with non-Newtonian fluids, as described by the Carreau model [60]. The heat transfer properties are critical due to thermal generation during surface contact, which affects the temperature of the lubricant film. However, temperatures are maintained at specific values during the wear cycle, allowing for isothermal simulations. Under high loads, lubricant film pressures can exceed 200 MPa, necessitating the use of the Barus model [61] to illustrate the relationship between dynamic viscosity and pressure.

In tribological evaluations, the CoF is essential for simulating lubricant behaviour in mixed lubrication conditions. The mini traction machine (MTM) at the Repsol Technology Lab is used to measure CoF across various shear rates, temperatures, and loads, with average CoF values employed for the three candidates during mixed lubrication, presented in previous works [62, 63]. For the boundary lubrication regime, a common CoF of 0.2 is applied to all oils to represent critical wear conditions, facilitating the calculation of asperity tangential shear stress on the journal bearing.

Cavitation poses a significant threat to rotating components, resulting in erosion and pitting damage. The phenomenon of cavitation is primarily influenced by the vapor pressure of the oil, which determines the transition point from liquid to vapor under varying pressure conditions. Cavitation typically occurs at sites of low- and high-pressure gradients, such as in connecting rod bearings and oil pumps.

In motorsport lubrication systems, another concern is oil aeration, characterized by an excessive air content in the oil that exceeds its gas saturation limit, commonly leading to foam formation in the oil pan. This aeration can induce critical issues, including oil starvation and exacerbated cavitation [7], which can cause severe engine damage. Furthermore, the oil gas saturation limit describes the maximum amount of air the oil can retain under steady-state conditions and can be quantified using the Bunsen coefficient, which assesses gas solubility in liquids as per ASTM D 2780 [64]. This coefficient facilitates the comparative analysis of different oil formulations used in the study, as detailed in Table 5.

3.3 Surface roughness characterization

Surface characteristics in high-performance engines usually differ from those in road applications. High loads and dynamic movement are mitigated with softer overlays that rapidly adapt the clearance in the contact areas, known as sputter bearings, typically composed of three different materials. This process is carried out during the running-in stage, where the engine is operated at a constant speed for a specific period to establish the working clearance. This procedure performs a controlled wear stage before the real working scenario, where the boundary conditions are more severe.

In this study, the method proposed in Ref. [50] is used to obtain the roughness parameters of a connecting rod bearing from a high-performance engine. Figure 18 depicts the surface roughness of a 3D topography of the bearing.

Initial surface roughness parameters obtained in this topography are shown in Fig. 18, where σ is the standard deviation of asperity peaks, β is the mean radius of curvature of the asperity peaks, η is the density of asperity peaks, and Z_s is the mean height of asperity peaks.

Table 5 Oil vapor pressure and aeration properties

	Temp. (°C)	Oil A	Oil B	Oil C
Vapor pressure (Pa)	50	80	53	53
	100	333	293	293
	150	933	1,600	1,600
Bunsen coefficient	25	0.132	0.137	0.136

3.4 Bearing material

The properties of bearing materials are crucial in determining their ability to withstand repeated impacts without failure, a measure known as ultimate resilience, which is influenced by yield strength, ultimate tensile strength, and elastic modulus. High-performance engines operate under severe conditions, with reciprocating motion supported mainly by bearings. Consequently, reliability issues have spurred research into advanced materials to enhance performance and durability. Commonly utilized in high-power density engines are 2-layer and 3-layer metal bearings, as illustrated in Fig. 19 from Ref. [5]. These bearings feature overlays that facilitate a non-aggressive running-in process, with electroplated overlays approximately 20 μm thick. The lining layer, approximately 200 μm thick, bonds the backing material to the overlay. In contrast, the backing metal, around 2 mm thick, reinforces the bearing shell and ensures proper positioning within the connecting rod. Elevated temperatures significantly reduce lubricant viscosity and promote mixed lubrication conditions, with Cu alloys offering superior thermal conductivity for effective heat dissipation.

In this case study, a 2-layer metal bearing is used in the connecting rod bearing, where the Pb-plating is a PbIn alloy, and the Cu alloy is known as Corson alloy (NC50). The properties of this material are presented in Table 6.

Critical data for the development of the cavitation erosion model were unavailable, necessitating the use of general

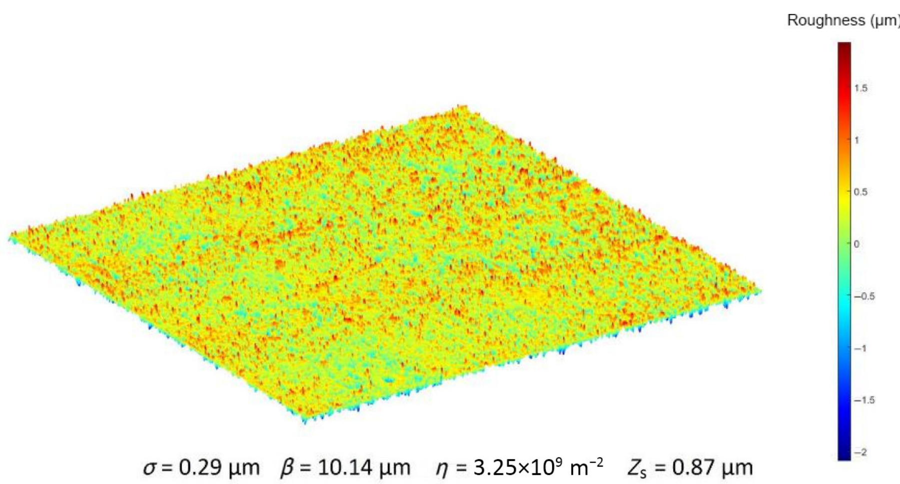

Fig. 18 Journal bearing 3D topography.

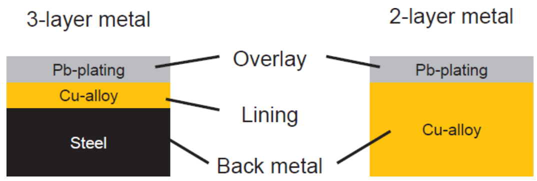

Fig. 19 Connecting rod bearing shell materials [5].

Table 6 Bearing shell material properties

Material	UTS (MPa)	0.2% Y_s (MPa)	E (GPa)	ε_{cav}	Y_f (MPa)
PbIn	—	—	40	0.3	100
Corson alloy (NC50)	690	590	120	—	—

assumptions derived from fatigue studies [65] to estimate values for the coating layer. The fatigue strength of electroplated PbIn was referenced from Ref. [7], with the UTS posited as double the fatigue strength (Y_f), yielding a value of 200 MPa. This UTS will be employed to calculate the EF of the coating. The yield strength (Y_s) of the PbIn coating was assumed to be 1.6 times of Y_f, resulting in a value of 160 MPa. This yield strength is crucial for assessing the pressure impacts from vapor bubble implosions, which are significant in accumulating cavitation energy. The mechanical properties of the coating are essential for understanding cavitation erosion in bearings, as they define the limits of energetic damage theories proposed in this investigation. Further exploration of the mechanical properties of engine bearings is recommended to build a comprehensive database.

3.5 Dynamic cycle

This study examines the dynamic behavior of a 4-stroke engine, which completes its intake, compression, combustion, and exhaust stages over a period of 2 revolutions (720°). High-performance engines are distinguished by their elevated rotational speeds, which maximize power output and generate significant inertial forces. These forces result in highly dynamic loads at the journal bearing, leading to unstable oil film conditions and high-pressure gradients over short time frames. In such environments, lubricants, despite their low vapor pressures, experience phase changes multiple times per cycle. Given that the engine operates at speeds exceeding 10,000 r/min, dynamic cycle durations are typically under 1 ms. To effectively evaluate cavitation erosion, simulations will be conducted at different engine speeds, with a maximum limit of 14,000 r/min imposed by balancing constraints in single-cylinder engines. However, for the assessment of cavitation damage, higher rotation rates will also be taken into consideration. Results from the lubrication system simulation under 100% engine load are illustrated in Fig. 20.

To enhance the importance of inertial load within rotational speed, Fig. 21 shows a polar plot of the bearing load at different

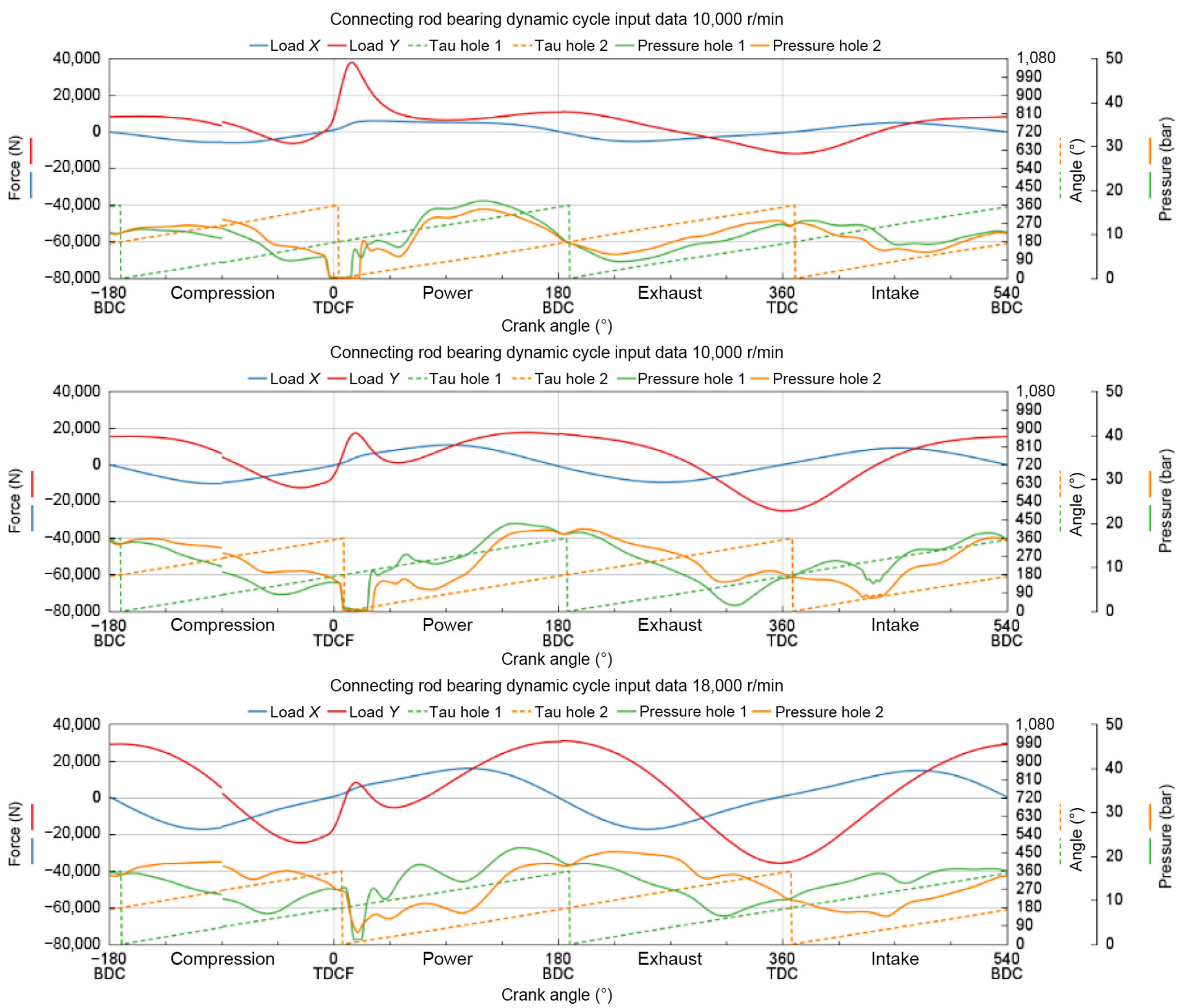

Fig. 20 Connection rod bearing dynamic cycles: (top) 10,000 r/min, (middle) 14,000 r/min, and (bottom) 18,000 r/min.

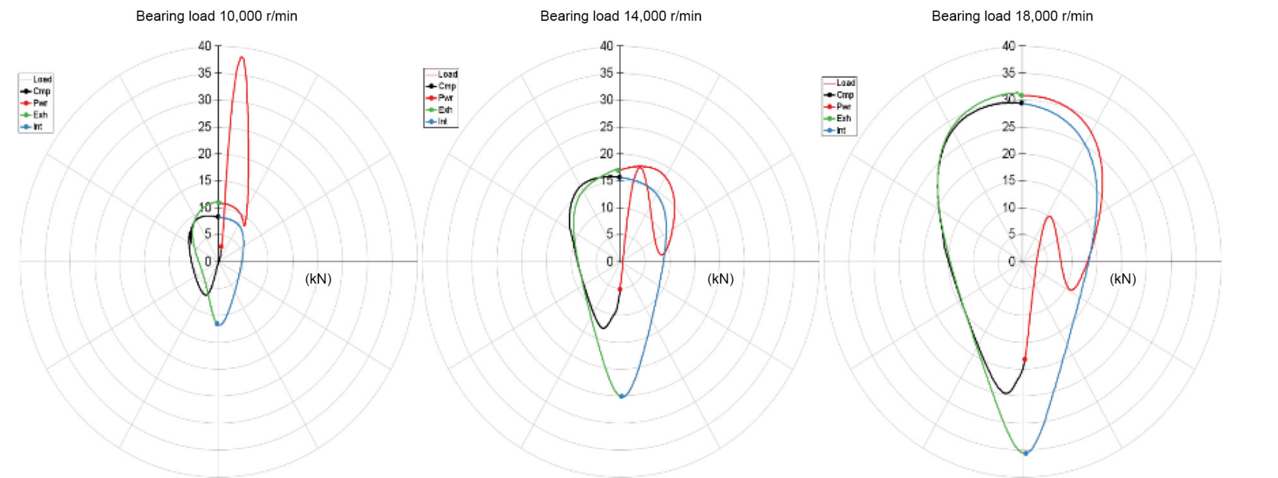

Fig. 21 Journal bearing load in polar coordinates: (left) 10,000 r/min, (middle) 14,000 r/min, (right) 18,000 r/min.

speeds, where the load is split in various colors depending on the stroke: blue is intake, black is compression, red is combustion, and green is exhaust.

3.6 Results

This section will present the results of the cavitation erosion model applied to a high-performance engine. Several assessments are conducted to evaluate the impact of various parameters on cavitation damage. First, an experimental correlation with a real connecting rod bearing at the end of its lifetime is presented to validate the damaged area due to cavitation erosion. Secondly, a multi-parameter study is presented to assess the damage. The variables used are bearing clearance, oil temperature, engine speed, and oil formulation. Then, a cavitation erosion evolution is presented to evaluate the variation in surface roughness within cavitation damage and how surface topography is modified due to oil vapor bubble implosions.

3.6.1 Experimental damage area validation

A correlation of cavitation damage area is carried out with data from another racing ICE to ensure a representative evaluation of cavitation erosion in high-performance engine bearings. As the engine characteristics and working conditions are different, the results are not expected to match them. However, from a comparative point of view, cavitation damage is typically observed in high-performance engines, which is a relevant finding to present as an outcome of this novel cavitation damage algorithm. The data from the simulation is an iterative case of the dynamic cycle at 18,000 r/min with Oil A at 100 °C for 1 h.

Figure 22 depicts a damage comparison with experimental data. It reveals that the dynamics of similar engines tend to form critical cavitation conditions in similar regions when subjected to highly dynamic scenarios. Therefore, the cavitation damage energy prediction correlates with experimental evidence.

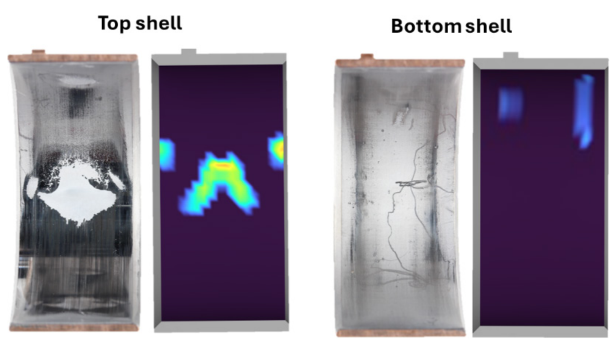

Fig. 22 Validation of cavitation damage area using experimental data.

The damage mechanism observed in the experimental data is a combination of wear and cavitation erosion. The repetitive erosive impacts from the collapses of cavitation bubbles fatigue the material surface until an initial layer of the coating, several microns thick, is completely removed. The surrounding area has experienced severe mixed lubrication conditions, resulting in high temperatures and degradation of the material coating. This validation of experimental damage serves as a verification step for the area of damage predicted by this novel MCE model. This study aims to present the numerical method and the novelty of the MCE model, which quantitatively predicts cavitation erosion in journal bearings of high-power-density engines. Complete validation of this numerical model requires further investigation using laboratory equipment to compare erosive rates, pitting depths, oil vapor distribution, and the energy-to-failure threshold, which cannot be measured in engines during normal operating conditions.

3.6.2 General cavitation damage results along the dynamic cycle

As the proposed algorithm generates dynamic data over time, a brief discussion on the time evolution of different variables is provided to enhance the understanding of the methodology. A single scenario will be presented, as the amount of data is too large to include a comparative analysis with different scenarios. Oil A is simulated at 100 °C and an engine speed of 18,000 r/min. Several variables will be shown at different instants of the combustion cycle. They are selected by crank angle (following the nomenclature in Fig. 20): −130°, −35°, 140°, and 320° (Figs. 23–26). These instants were selected in specific cavitation events to understand the damage accumulation due to bubble implosions, among other hydrodynamic and lubricant variables.

To address the damage potential of the complete dynamic cycle, a time average of the transient variables is computed and shown in Fig. 27, where the regions with more aggressive cavitation show a clear correlation with low film fraction, high vapor bubble impact pressure, and a significant gradient in the hydrodynamic pressure as well as density and viscosity.

3.6.3 Cavitation damage energy assessment

Cavitation damage can be caused by many factors, including the application, working fluid, working conditions, and ICE setup. To address the sensitivity of the proposed cavitation damage model, several scenarios will be compared to highlight the relevant

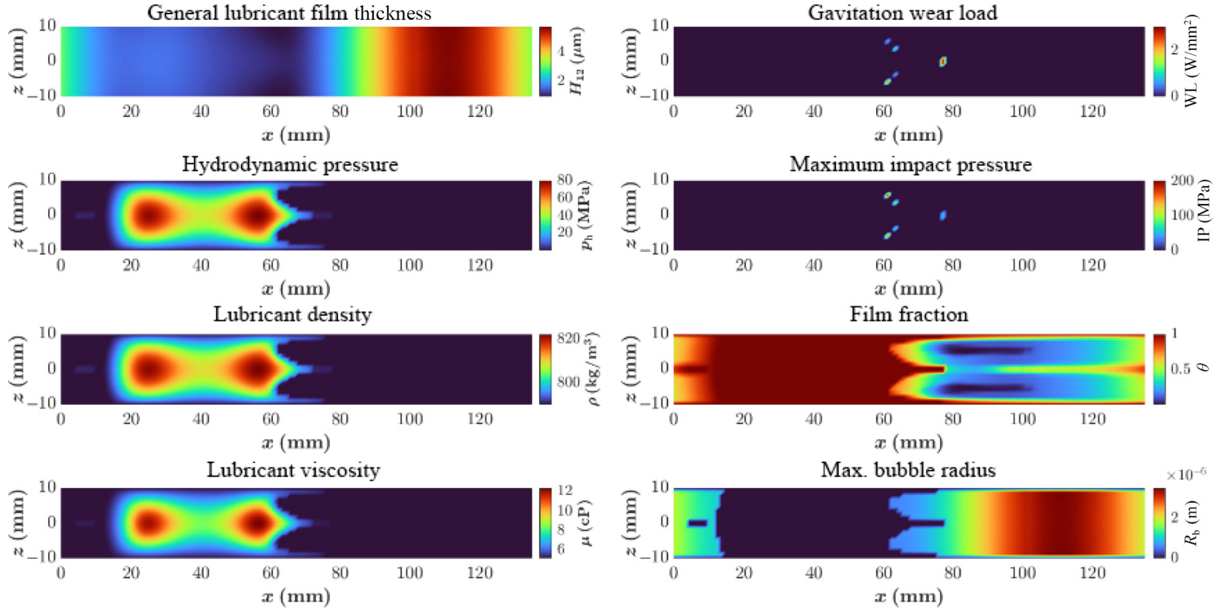

Fig. 23 Dynamic variables from the M-EHL simulation at −130° crank angle.

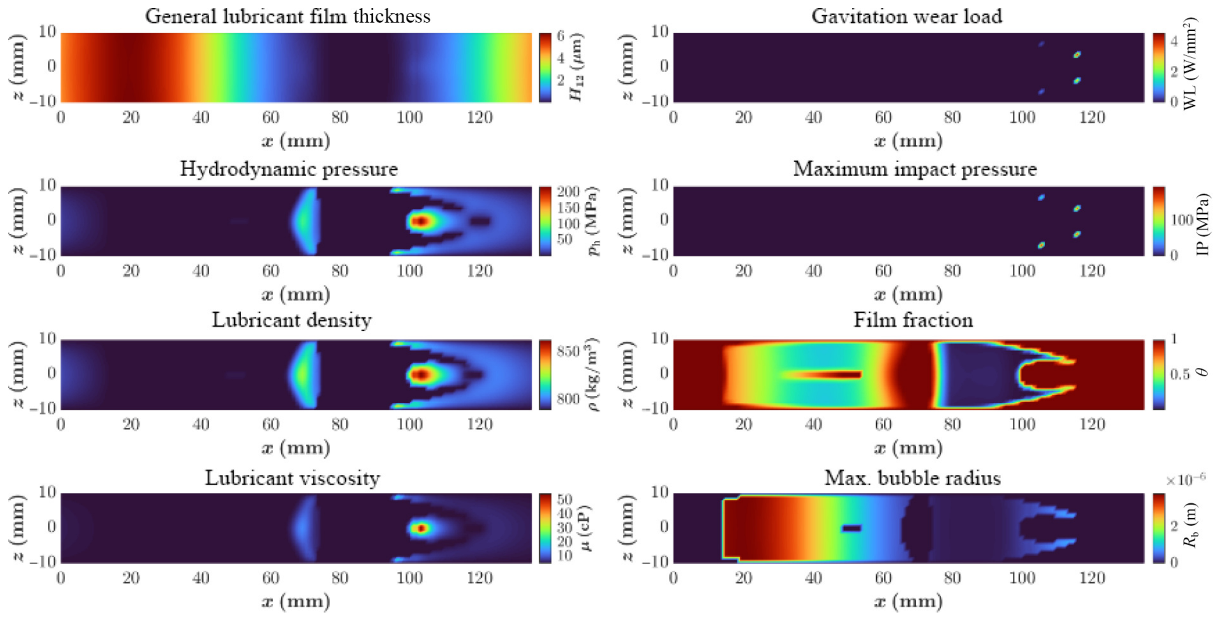

Fig. 24 Dynamic variables from the M-EHL simulation at −35° crank angle.

differences in the energy accumulated in the cavitation damage. The dynamic cycles used are those exported from the 1D lubrication system simulation. The accumulation of cavitation damage energy is directly related to the cavitation aggressiveness in the region. This is because the energy only accumulates in the hydrodynamic node once the maximum impact pressure overcomes the yield strength of the material (in this case, 160 MPa). This conditional relationship is crucial for predicting damaged areas in real-world scenarios. Once the cavitation damage energy exceeds the material's failure energy, the erosion process begins, removing bearing material according to the erosion propagation algorithm.

Engine load is a relevant variable in engine performance; however, a clear relationship was not found between engine load and cavitation damage. Therefore, it is not included as a variable in this sensitivity study.

3.6.3.1 Lubricant formulation

The lubricant formulation has a significant impact on the properties, as described in Section 4.2. Some additional relevant properties related to cavitation include vapor pressure, Bunsen coefficient, viscosity, and density. Therefore, an assessment of three different ultralow-viscosity lubricant formulations is presented, and the oil properties are included in Section 4.2.

Similar damaged areas can be observed in Fig. 28 for the three lubricants. However, the cavitation aggressiveness has significant differences. Oil C shows the highest results of accumulated cavitation damage energy, followed by Oil B and Oil A. All three lubricant results exceed the 10 J/mm^2 energy-to-failure threshold of the material, indicating that erosion is expected in these areas. This outcome means that in the same performance scenario, Oil C will cause more erosion damage in the bearing due to its slightly larger damaged area and significantly higher accumulated damage energy. Oil A will provide better protection against cavitation damage, but some erosion damage is expected.

3.6.3.2 Oil temperature

Experimental evidence is presented in Section 4.2 for the

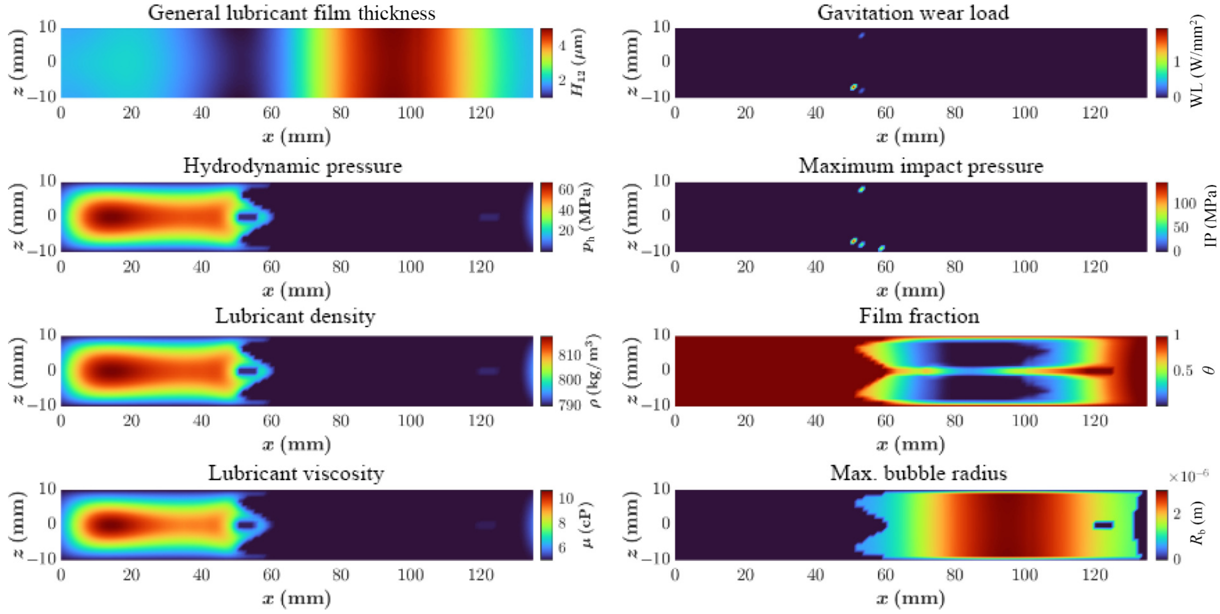

Fig. 25 Dynamic variables from the M-EHL simulation at 140° crank angle.

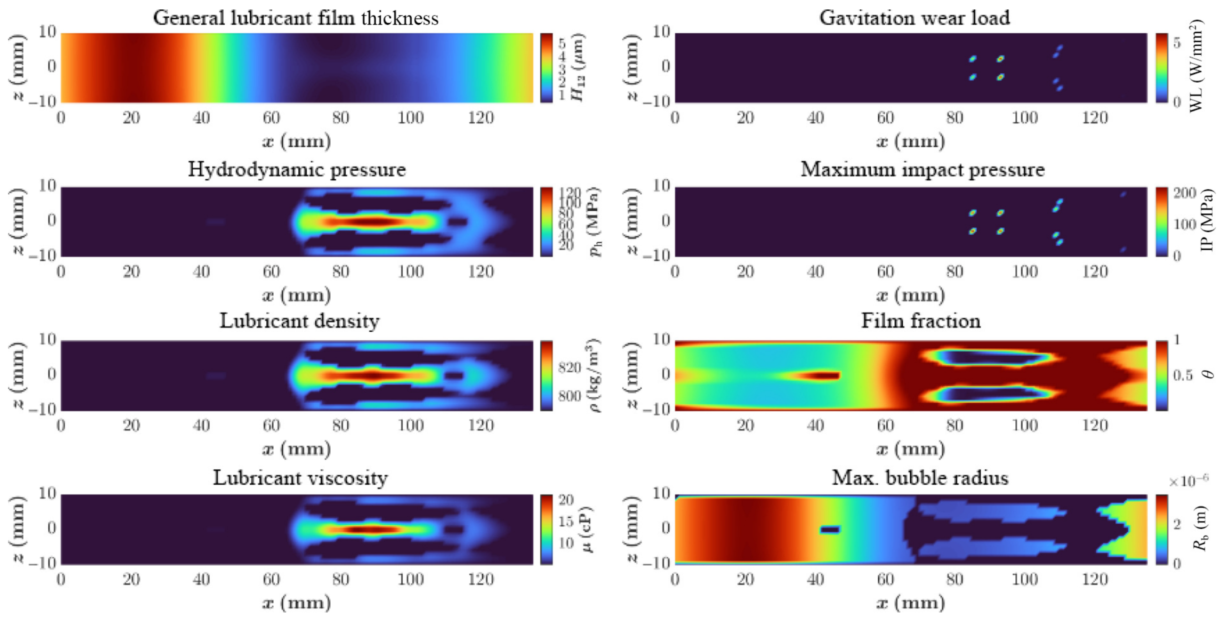

Fig. 26 Dynamic variables from the M-EHL simulation at 320° crank angle.

dependency of vapor pressure on oil temperature. As the lubricant temperature increases, so does the vapor pressure. This scenario is significantly more critical due to the higher probability of cavitation. Therefore, as this point is especially relevant in motorsport applications, three different temperatures are studied: 80, 100, and 150 °C. The lubricant selected for this specific comparison is the one that presented the most variability in vapor pressure with temperature. In this case, Oil B and Oil C show the same values due to their similar base oil. Oil B was selected due to its lower viscosity, which becomes critical at high temperatures and causes the oil film to break up.

Concerning the temperature influence on cavitation erosion, it can be noticed in Fig. 29 that with the increase in oil temperature, the accumulated erosion energy on the bearing shell increases. Therefore, it can be concluded that working temperature is a critical parameter to avoid excessive damage caused by cavitation. However, the three temperature cases exceed the engine-to-failure threshold, which causes imminent bearing erosion.

3.6.3.3 Engine speed

As explained in this study, cavitation becomes more aggressive as the flow speed increases. In the case of ICE, this is directly correlated with engine speed, which becomes critical when reaching a certain threshold, as studied by several authors [45, 66, 67]. Therefore, as this point is especially relevant in motorsport applications, three different engine speeds are considered: 10,000, 14,000, and 18,000 r/min. In the case of NSF250R ICE, 18,000 r/min exceeds the engine speed limit due to the complexity of load balance for a single-cylinder engine. However, these engine speeds are typically found in multicylinder ICEs from other motorsport categories, so the study of this higher regime is conducted to consider a broader range of engines in the cavitation damage assessment. The lubricant selected for this comparison is based on the viscosity variability with shear rate, which is directly related to the engine speed. In this case, Oil C presents a higher variability of dynamic viscosity. Oil temperature will be set to 100 °C.

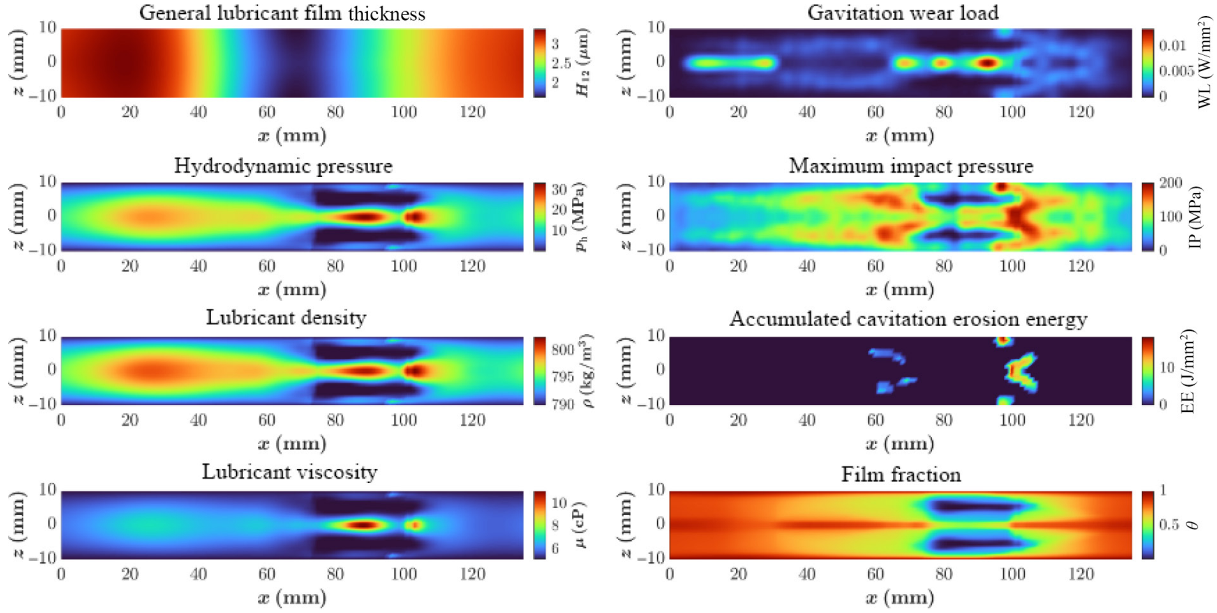

Fig. 27 Average values along the dynamic cycle from the M-EHL simulation.

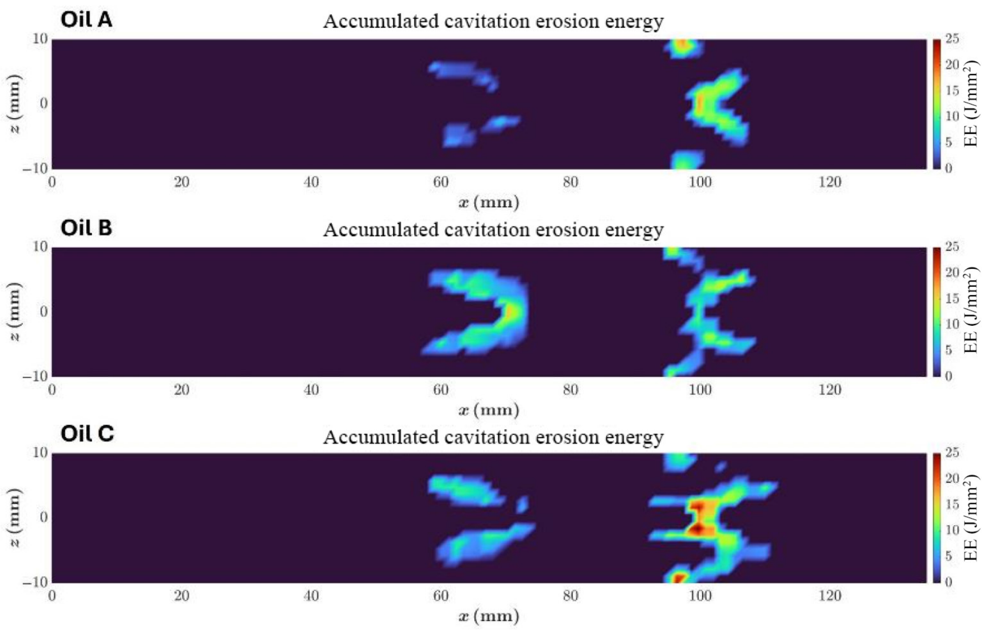

Fig. 28 Accumulated cavitation damage energy computed in three different lubricant formulations at 100 ºC, 18,000 r/min, and 100% of engine load for 1 h.

Figure 30 shows a clear tendency in the engine speed during aggressive cavitation erosion. Therefore, it can be concluded that the same findings about cavitation aggressiveness with flow velocity reported by authors in other applications can be observed in ICE applications [43]. In this scenario, the approximate relative velocities in the connecting rod bearing are 20 m/s at 10,000 r/min, 30 m/s at 14,000 r/min, and 40 m/s at 18,000 r/min.

3.6.3.4 Journal bearing clearance

Limiting journal bearing clearance has been promoted for decades by ICE specialists and racing teams as a solution for cavitation damage. This assumption is correct due to the following considerations: the thinner the bearing clearance, the lower the orbital movement of the journal, which reduces the dynamic oscillation of the mechanism. However, it can cause tribological wear due to an insufficient oil film thickness and a reduced hydrodynamic effect. As this case is relevant in motorsport applications, four different journal bearing clearances will be considered to assess cavitation damage. The lubricant selected for this specific comparison is based on the critical accumulation of cavitation damage energy, as this comparison aims to achieve a solution for cavitation damage. Therefore, Oil B is selected as a working fluid, and the oil temperature will be set to 100 ºC. All previous case setups are run with a radial clearance of 50 μm. In this case, three more setups are added: 40, 30, and 20 μm.

Figure 31 shows the different accumulated cavitation damage energies with different journal bearing clearances, going from 50 to 20 μm. The observed tendency is less aggressive cavitation in terms of maximum values; however, it increases in the damaged area with the reduction in clearance. In all cases, some damage is still expected due to cavitation erosion. Therefore, based on the results obtained, it cannot be confirmed that bearing clearance reduction eliminates cavitation damage. However, it does reduce the aggressiveness, as shown in Fig. 31.

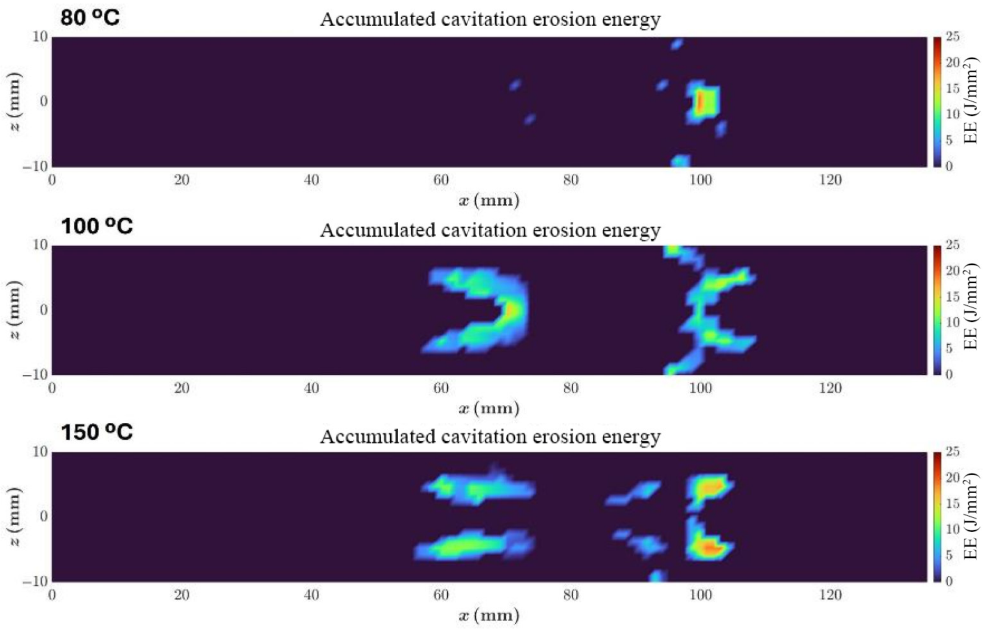

Fig. 29 Accumulated cavitation damage energy for Oil B computed at three different temperatures: 80, 100, and 150 ºC, with an engine speed maintained at 18,000 r/min and 100% of engine load over 1 h.

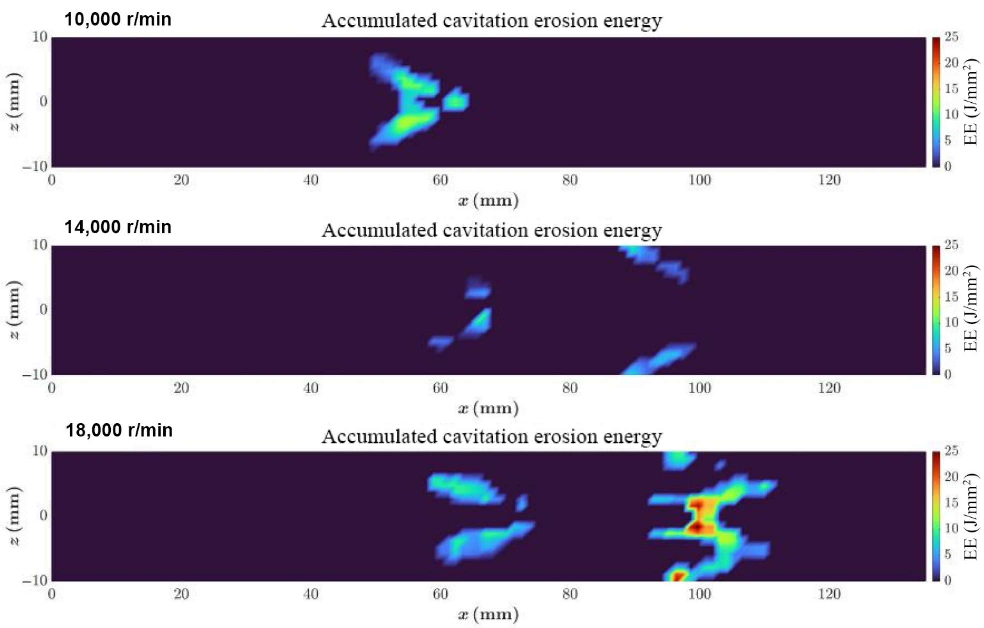

Fig. 30 Accumulated cavitation damage energy for Oil C at 100ºC across three different rotational speeds at 100 % of engine load: 10,000, 14,000, and 18,000 r/min, simulated for a 1 h run.

3.6.4 Cavitation erosion evolution

The process of cavitation erosion is a complex phenomenon characterized by multiple physical interactions associated with material removal, including heat transfer, phase change, fatigue, and elastic and plastic deformations, among others. This study proposes an MCE model, which involves two stages. In the first stage, the model computes the accumulated cavitation damage energy at the macroscale level. Once the material's energy-to-failure threshold is surpassed, the second stage initiates the material removal process, characterized by the formation of spherical pits at the microscale. The erosion propagation algorithm incrementally adjusts the shape of the pits as the accumulated cavitation damage energy increases, ultimately reaching a maximum pit size limit. Given that cavitation erosion is predominantly influenced by the surface material properties, variations in surface roughness will be examined for Oil C, under the conditions outlined in the previous subsection: an oil temperature of 100 ºC, an engine speed of 18,000 r/min, a radial clearance of 50 μm, and a duration of one hour. The selected area for this investigation is depicted in Fig. 32.

Figure 33 illustrates the accumulated cavitation damage energy and the evolution of pit spherical caps within a single node over one hour. The accumulated energy surpasses the energy threshold for material failure after 1,800 s, indicating the initiation of material removal at the bearing surface. Once this threshold is exceeded, the structural integrity of the bearing surface undergoes a dramatic decline, resulting in an almost exponential increase in material erosion.

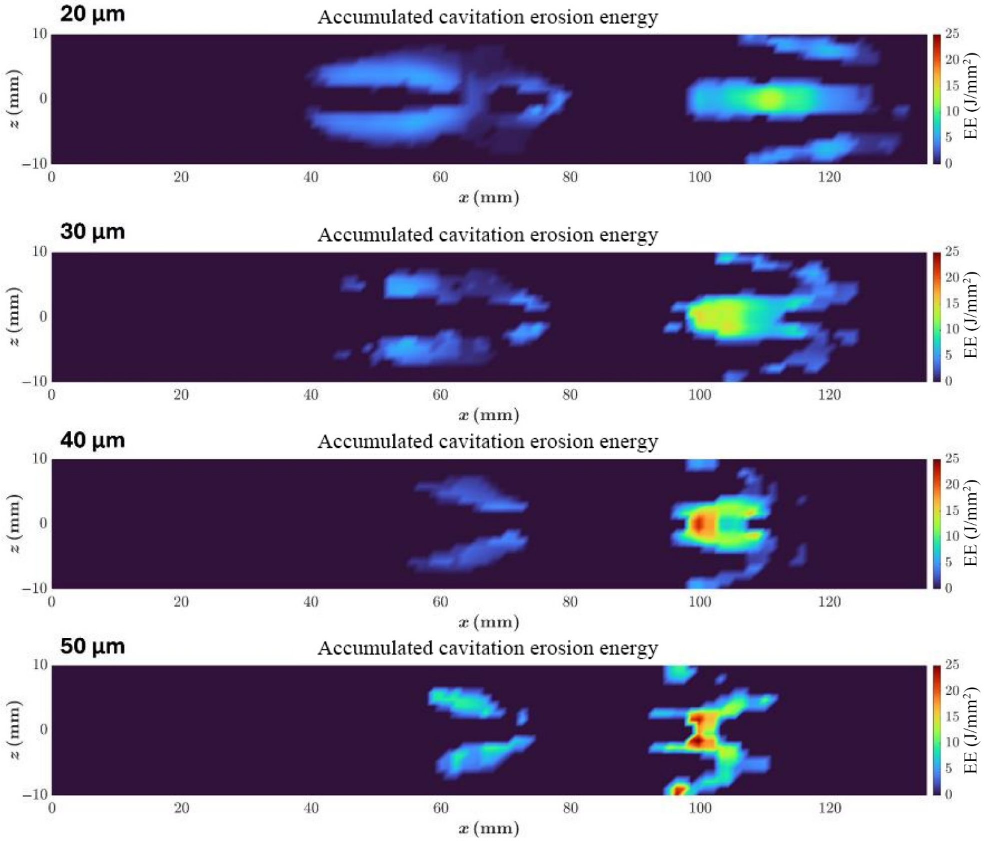

Fig. 31 Accumulated cavitation damage energy computed for Oil B at 100 °C, 18,000 r/min, and 100% of engine load. Four different radial clearance setups are simulated for a 1 h period.

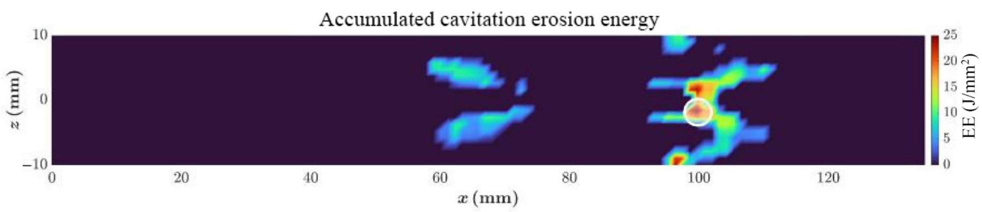

Fig. 32 Local bearing area selected (highlighted in white) to study microscale cavitation erosion at the bearing surface.

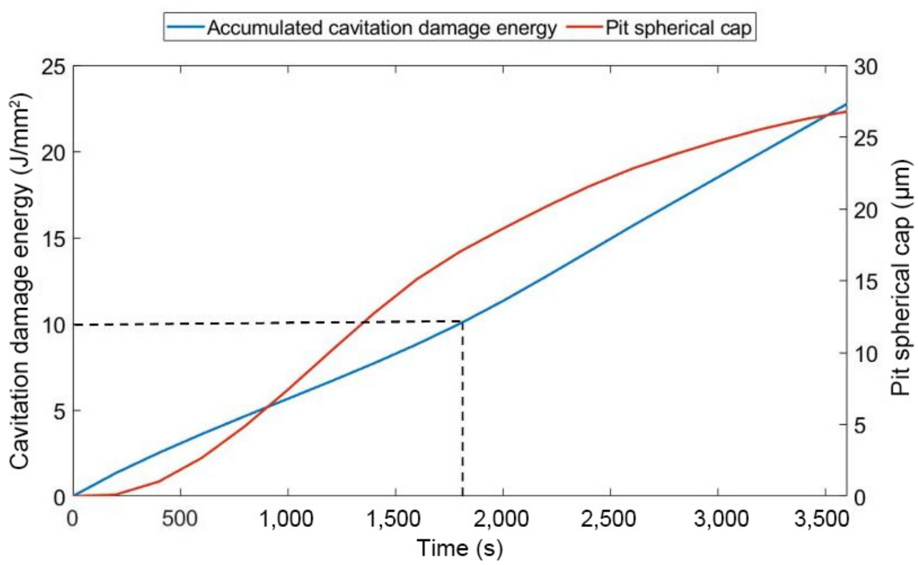

Fig. 33 Accumulated cavitation damage energy and evolution of the spherical cap pit.

清華大学出版社 Tsinghua University Press | SciOpen

To explain the evolution of erosion at the microscale, the topography of the bearing surface will be presented at various stages of cavitation corresponding to a specific node area within the journal bearing (Fig. 34). Erosion initiates with the formation of small pits after approximately 30 min of operation. Subsequently, the depth and diameter of these pits increase as damage propagates across the surface. The 1 h mark indicates significant material loss, consistent with the ongoing cavitation erosion process.

Cavitation erosion is an iterative process that occurs over time, leading to a time evolution of the roughness parameters defined by the Greenwood–Tripp equation, which is calculated with the method proposed in Ref. [50]. This time evolution, illustrated in Fig. 35, highlights the intricate dependencies involved in cavitation erosion. As the surface becomes increasingly rough, the parameters exhibit variable trends.

The standard deviation of peak height (Sigma) and mean peak height (Z_s), both indicative of peak height distribution, initially decrease before undergoing a significant increase. This behavior is attributed to the geometry of the pits, which are indentations that make the material highly irregular in terms of height distribution.

In contrast, the mean peak radius of curvature (Beta) displays a downward trend as the summits of the peaks sharpen due to the erosive process. Once all prominent peaks are eroded, Beta will increase sharply, reflecting the formation of a plateau following the removal of the initial material.

Additionally, peak density (E_{ta}) demonstrates a clear upward trend, which can be ascribed to the rougher characteristics of the remaining surface. E_{ta} is anticipated to continue increasing until the material is sufficiently eroded, decreasing dramatically as the newly exposed surface transitions into a plateau formation.

4 Conclusions

This research work presents a novel MCE model applied to

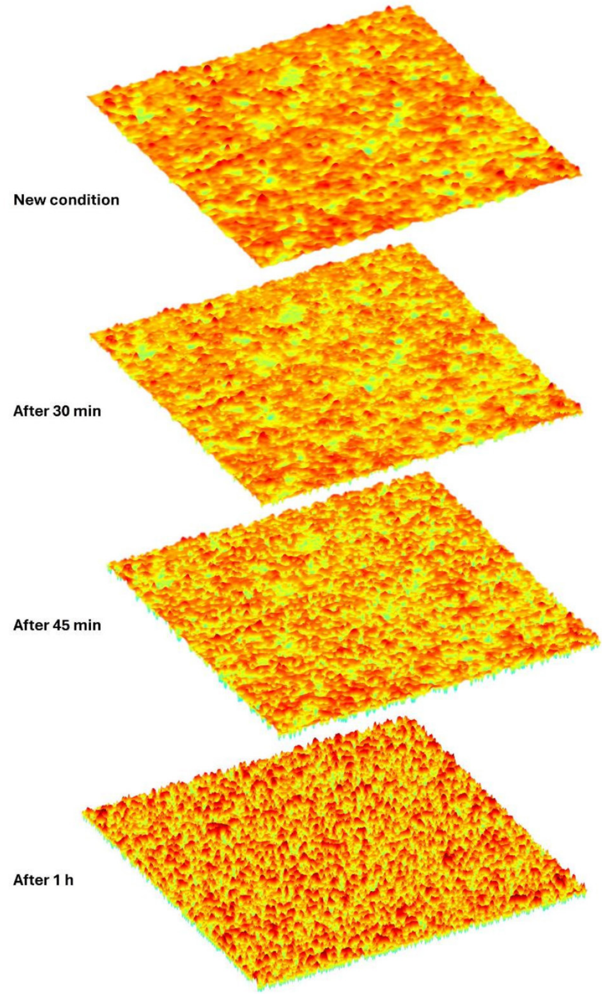

Fig. 34 Surface bearing erosion at different time frames.

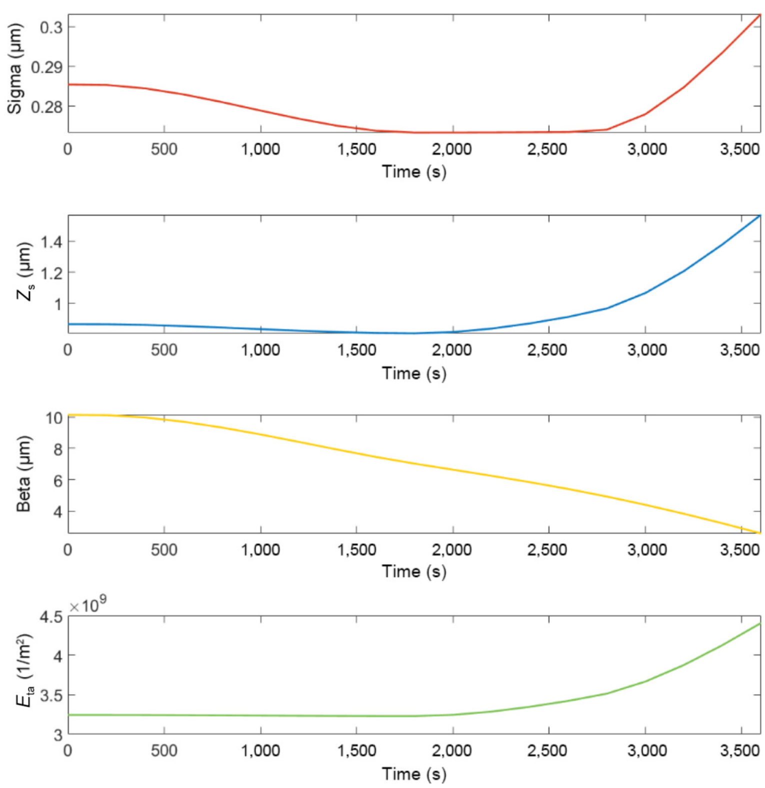

Fig. 35 Evolution of roughness parameters during the cavitation erosion process.

journal bearings in high-power-density ICEs. The proposed model offers a comprehensive framework for calculating cavitation damage energy at the macroscale while capturing erosion propagation at the microscale. The model predicts cavitation damage based on a mixed-elastohydrodynamic lubrication model that integrates various assumptions about oil vapor bubbles within the lubricating film. This approach provides a comprehensive solution to a complex 3D problem, enabling the assessment of erosion damage without the high computational costs typically associated with 3D-CFD simulations.

Cavitation erosion is quantified through an iterative algorithm that modifies the surface topography at the microscale. The propagation of erosion is based on the accumulated cavitation damage energy calculated on the hydrodynamic mesh in the macroscale. A specific case study of a high-performance engine is presented, where transient results are derived from high-performance combustion cycles under varying performance scenarios. These dynamic cycles are modeled using a 1D lubrication system simulation that includes all mechanical components and lubrication circuits. This yields a comprehensive understanding of the transient variability inherent in this engine type, enabling a detailed investigation into cavitation damage within the connecting rod sliding bearing.

A detailed mixed elastohydrodynamic lubrication simulation of the connecting rod bearing was conducted to investigate local phenomena associated with cavitation. First, the predicted cavitation-damaged areas are compared with experimental data to verify the MCE model's predictions. Second, a sensitivity analysis is performed to evaluate the model's predictions under different boundary conditions, including variations in lubricant formulations, oil temperature, engine speed, and journal bearing clearance. Lastly, the surface topography results, which eroded after one hour of engine operation, underscore the significance of cavitation damage in high-performance ICEs. Additionally, a comparative analysis of the time evolution of the roughness parameters for the three lubricants is presented to assess the aggressiveness of cavitation over time.

Acknowledgements

We would like to express our gratitude to our partners from Repsol SA, who finance this research and contribute to developing new lubricant formulations through simulation tools. Furthermore, we would like to express our gratitude to all the colleagues from CINTECX and the University of São Paulo who contributed to this research's success. F. J. Profito recognizes that this study was financed, in part, by the São Paulo Research Foundation (FAPESP), Brazil. Process Number #2022/03110-0.

Availability of data and materials

The data that support the findings of this study are available from the corresponding author upon reasonable request.

Declaration of competing interest

The authors have no competing interests to declare that are relevant to the content of this article.

References

[1] Kalogiannis K, Desai P, Mian O, Mainwaring R. Simulated bearing durability and friction reduction with ultra-low viscosity oils. In: Proceedings of the International Powertrains, Fuels & Lubricants Meeting, 2018.

[2] Zoli G, Turner M, Newman C. Highly efficient lubricant for sport motorcycle application—Fuel economy and durability testing. *SAE Int J Fuels Lubr* **6**: 986–994 (2013)

[3] Kurotani T, Kuzuoka K, Kudo H. Research on engine controll to make effective use of bioethanol-blend fuels. *Honda R& D Technical Review* **26**(1): 110–117 (2014)

[4] Information on https://kipdf.com/engine-bearing-failure-analysis-and-correction_5ad1e8817f8b9a718d8b45b0.html

[5] Honda Motor Co. Ltd. *Honda R&D Technical Review F1 Special (The 3rd Era Activities)*. Tokyo (Japan): Honda Motor Co., Ltd, 2009.

[6] Taylor R I. Lubrication, tribology & motorsport. In: Proceedings of Motorsports Engineering Conference & Exhibition, Indiana, USA, 2002.

[7] Garner D R, James R D, Warriner J F. Cavitation erosion damage in engine bearings: Theory and practice. *J Eng Gas Turb Power* **102**(4): 847–857 (1980)

[8] Franc J P, Michel J M. *Fundamentals of Cavitation*. Dordrecht (the Netherlands): Springer, 2005.

[9] Dular M, Coutier-Delgosha O. Numerical modeling of cavitation erosion. *Int J Numer Meth Fl* **61**(12): 1388–1410 (2009)

[10] Plesset M S, Prosperetti A. Bubble dynamics and cavitation. *Annu Rev Fluid Mech* **9**: 145–185 (1977)

[11] Zgolli R, Bel Hadj Taher A, Ennouri M, Kanfoudi H. Homogeneous cavitation model used to predict erosion. In: *Proceedings of the 10th International Symposium on Cavitation*. Katz J, Ed. New York: ASME Press, 2018: 14–16

[12] Magnotti G M, Battistoni M, Saha K, Som S. Development and validation of the cavitation-induced erosion risk assessment tool. *Transport Eng* **2**: 100034 (2020)

[13] Gómez-Molina P, Sanz-Lorenzo L, Carpio J. An efficient numerical algorithm to solve hydrodynamic lubrication problems with cavitation. *Comput Meth Appl M* **433**: 117470 (2025)

[14] Maassen F, Koch F, Pischinger F. Connecting rod bearing operation with aerated lube oil. In: Proceedings of the International Fuels & Lubricants Meeting & Exposition Michigan, USA, 1998: 981404.

[15] Brennen C E. *Cavitation and Bubble Dynamics*. Cambridge (UK): Cambridge University Press, 2013.

[16] Franc J P. Physics and control of cavitation. *Physics and Control of Cavitation. Educational Notes RTO-EN-AVT-143*. Paper 2, 2-1–2-36, 2006.

[17] Braun M, Pierson K, Snyder T. Two-way coupled Reynolds, Rayleigh-Plesset-Scriven and energy equations for fully transient cavitation and heat transfer modeling. *IOP Conf Ser-Mat Sci* **174**: 012030 (2017)

[18] Braun M J, Hannon W M. Cavitation formation and modeling for fluid film bearings: A review. *P I Mech Eng J-J Eng* **224**(9): 839–863 (2010)

[19] San Andrés L. *Liquid Cavitation in Fluid Film Bearings*. The OAKTrust Digital Repository, 2009.

[20] Fivel M, Franc J P, Chandra Roy S. Towards numerical prediction of cavitation erosion. *Interface Focus* **5**(5): 20150013 (2015)

[21] Peters A, el Moctar O. Numerical assessment of cavitation-induced erosion using a multi-scale Euler–Lagrange method. *J Fluid Mech* **894**: 19 (2020)

[22] Wang T H, Chen L Y. Thermodynamic behavior and energy transformation mechanism of the multi-period evolution of cavitation bubbles collapsing near a rigid wall: A numerical study. *Energies* **16**(3): 1048 (2023)

[23] Fortes Patella R, Choffat T, Reboud J L, Archer A. Mass loss simulation in cavitation erosion: Fatigue criterion approach. *Wear* **300**(1–2): 205–215 (2013)

[24] Franc J P. The Rayleigh-Plesset equation: A simple and powerful tool to understand various aspects of cavitation. *Fluid dynamics of cavitation and cavitating turbopumps* **496**: 1–41 (2007)

[25] Blanco-Rodríguez J, Cortada-Garcia M, Profito F J, Porteiro J. A novel multiscale contact mechanics approach for wear prediction in

journal bearings via a mixed elastohydrodynamic simulation. *Lubricants* **13**(5): 230 (2025)

[26] Blanco-Rodríguez J. On the development of a comprehensive damage prediction algorithm for mixed-elastohydrodynamic lubrication conditions in high-power density engines. Ph. D. Thesis. Spain: University of Vigo, 2025.

[27] Profito F J, Zachariadis D C, Dini D. Partitioned fluid–structure interaction techniques applied to the mixed-elastohydrodynamic solution of dynamically loaded connecting-rod big-end bearings. *Tribol Int* **140**: 105767 (2019)

[28] Profito F J, Zachariadis D C. Partitioned fluid-structure methods applied to the solution of elastohydrodynamic conformal contacts. *Tribol Int* **81**: 321–332 (2015)

[29] Profito F J, Vlădescu S C, Reddyhoff T, Dini D. Transient experimental and modeling studies of laser-textured micro-grooved surfaces with a focus on piston-ring cylinder liner contacts. *Tribol Int* **113**: 125–136 (2017)

[30] Profito F J, Giacopini M, Zachariadis D C, Dini D. A general finite volume method for the solution of the Reynolds lubrication equation with a mass-conserving cavitation model. *Tribol Lett* **60**: 18 (2015)

[31] Plesset M S, Chapman R B. Collapse of an initially spherical vapour cavity in the neighbourhood of a solid boundary. *J Fluid Mech* **47**(2): 283–290 (1971)

[32] Rayleigh L. VIII. On the pressure developed in a liquid during the collapse of a spherical cavity. *Lond Edinb Dublin Philos Mag J Sci* **34** (200): 94–98 (1917)

[33] Steck B, Sommerfeld G, Schneider V. Cavitation on wet cylinder liners of heavy duty diesel engines. *SAE Technical Paper* 2006-01-3477 (2006)

[34] Singhal A K, Athavale M M, Li H Y, Jiang Y. Mathematical basis and validation of the full cavitation model. *J Fluid Eng-T Asme* **124**(3): 617–624 (2002)

[35] Markatos N C, Singhal A, Singhal K A. Numerical analysis of one-dimensional, two-phase flow in a vertical cylindrical passage numerical analysis of one-dimensional, two-phase flow in a vertical cylindrical passage. *Adv Eng Softw* **4**(3): 99–106 (1982)

[36] Millies M, Mewes D. Interfacial area density in bubbly flow. *Chem Eng Process* **38**(4–6): 307–319 (1999)

[37] Qiu N, Xu P, Zhu H, Zhou W J, Xun D B, Li M W, Che B X. Cavitation morphology and erosion on hydrofoil with slits. *Int J Mech Sci* **275**: 109345 (2024)

[38] Ochiai M, Sakai F M, Hashimoto H. Reproducibility of gaseous phase area on journal bearing utilizing multi-phase flow CFD analysis under flooded and starved lubrication conditions. *Lubricants* **7**(9): 74 (2019)

[39] Ochiai M, Sakai F M, Hashimoto H. The multiphase flow CFD analysis in journal bearings considering surface tension and oil-filler port flow. In: *Computational Fluid Dynamics Simulations*. Ji G Z, Zhu J J, Eds. UK: IntechOpen, 2020.

[40] Dular M, Požar T, Zevnik J, Petkovšek R. High speed observation of damage created by a collapse of a single cavitation bubble. *Wear* **418**: 13–23 (2019)

[41] Sagar H J, el Moctar O. Dynamics of a cavitation bubble near a solid surface and the induced damage. *J Fluid Struct* **92**: 102799 (2020)

[42] Kim K H, Chahine G, Franc J P, Karimi A. *Fluid Mechanics and its Applications Advanced Experimental and Numerical Techniques for Cavitation Erosion Prediction*. Germany: Springer, 2014.

[43] Fortes-Patella R, Challier G, Reboud J L, Archer A. Energy balance in cavitation erosion: From bubble collapse to indentation of material surface. *J Fluid Eng-T Asme* **135**(1): 011303 (2013)

[44] Lauterborn W, Lechner C, Koch M, Mettin M. Bubble models and real bubbles: Rayleigh and energy-deposit cases in a Tait-compressible liquid. *IMA J Appl Math* **83**(4): 566–589 (2018)

[45] Chahine G L. Modeling of cavitation dynamics and interaction with material. In: *Advanced Experimental and Numerical Techniques for Cavitation Erosion Prediction. Fluid Mechanics and Its Applications*. Kim K H, Chahine G, Franc J P, Karimi A, Eds. 2014: 123–161.

[46] Reboud J L, Fortes-Patella R, Challier G, Reboud J L, Archer A. Cavitation erosion mechanism: Numerical simulations of the interaction between pressure waves and solid boundaries. In: Proceedings of the CAV 2001 Symposium, 2001: hal-00211723.

[47] Zhang Z N, Pan S H, Yin N, Shen B, Song J. Multiscale analysis of friction behavior at fretting interfaces. *Friction* **9**(1): 119–131 (2021)

[48] König F, Ouald Chaib A, Jacobs G, Sous C. A multiscale-approach for wear prediction in journal bearing systems–from wearing-in towards steady-state wear. *Wear* **426–427**: 1203–1211 (2019)

[49] Pinto Carvalho R, Couto Carneiro A M, Andrade Pires F M, Doca T. An efficient multiscale strategy to predict the evolution of the real contact area between rough surfaces. *Tribol Int* **165**: 107255 (2022)

[50] García-Rodiño D, Blanco-Rodríguez J, Cortada-García M, Fernández S, Porteiro J. A numerical procedure for calculating roughness parameters for the Greenwood-Tripp model of asperity contact based on 3D measurements. *Tribol Int* **200**: 110156 (2024)

[51] Honda R&D Co. Ltd. Dossier de prensa NSF250R, 2011.

[52] Honda HRC. NSF250R Owner's Manual/Parts List, 2012.

[53] Blanco-Rodríguez J, Simón-Montero X, Cortada-García M, Maroto S, Porteiro J. Modeling the impact of reducing lubricant viscosity on a conventional passenger car fuel economy and wear protection. *Results Eng* **24**: 103159 (2024)

[54] Offner G. Modeling of condensed flexible bodies considering non-linear inertia effects resulting from gross motions. *P I Mech Eng K-J Mul* **225**(3): 204–219 (2011)

[55] Spikes H. Friction modifier additives. *Tribol Lett* **60**: 5 (2015)

[56] Zhao J, Huang Y Y, He Y Y, Shi Y J. Nanolubricant additives: A review. *Friction* **9**(5): 891–917 (2021)

[57] Meng Y G, Xu J, Ma L R, Jin Z M, Prakash B, Ma T B, Wang W Z. A review of advances in tribology in 2020–2021. *Friction* **10**(10): 1443–1595 (2022)

[58] Dubey M K, Chaudhary R, Emmandi R, Seth S, Mahapatra R, Harinarain A K, Ramakumar S S V. Tribological evaluation of passenger car engine oil: Effect of friction modifiers. *Results Eng* **16**: 100727 (2022)

[59] Ferrick K. Engine Oil Licensing and Certification System. *American Petroleum Institute*, 2010.

[60] Carreau P J. Rheological equations from molecular network theories. *T Soc Rheol* **16**(1): 99–127 (1972)

[61] Barus C. Isothermals, isopiestics and isometrics relative to viscosity. *Am J Sci* **S3–45**(266): 87–96 (1893)

[62] Blanco-Rodríguez J, Porteiro J, López-Campos J A, Cortada-García M, Fernández-Castejón S. Wear protection assessment of ultralow viscosity lubricants in high-power-density engines: A novel wear prediction algorithm. *Friction* **12**(8): 1785–1800 (2024)

[63] Blanco-Rodríguez J, Porteiro J, López-Campos J A, Domínguez B, Cortada-Garcia M. Friction assessment of ultralow viscosity lubricant formulations based on a validated elastohydrodynamic simulation. *Int J Engine Res* **24**(8): 3532–3543 (2023)

[64] American Society for Testing and Materials. Standard test method for solubility of fixed gases in liquids. ASTM D 2780, 2021.

[65] Pang J C, Li S X, Wang Z G, Zhang Z F. General relation between tensile strength and fatigue strength of metallic materials. *Mater Sci Eng A-Struct* **564**: 331–341 (2013)

[66] Patella R F, Challier G, Reboud J L, Archer A. Cavitation erosion mechanism: Numerical sumulations of the interaction between pressure waves and solid boundaries. In: Proceedings of the CAV 2001 Symposium, 2001: hal-00211723.

[67] Sarkar P, Ghigliotti G, Franc J P, Fivel M. Mechanism of material deformation during cavitation bubble collapse. *J Fluid Struct* **105**: 103327 (2021)

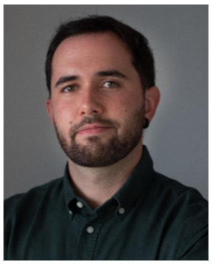

Javier Blanco-Rodríguez is a postdoctoral research engineer at GTE research group (CINTECX, University of Vigo, Spain). He has his Ph.D. and master degrees of science in industrial engineering and his bachelor degree in mechanical engineering, all at University of Vigo. He has got professional experience in R&D companies such as CTAG (Porriño, Spain) as student internship or AVL (Graz, Austria) doing his master thesis. Currently, he is team leader of a dedicated group to develop simulation models (GT-Suite, Matlab, and Converge CFD), experimental procedures, and data analysis for Repsol Technology Lab in several research projects. He is mainly focused on lubricant and fuel formulations optimization for motorsport applications, lubricant enhancement for road vehicles on WLTC & RDE performance assessment, and hybrid-ICE powertrain efficiency optimization on WLTC.

David García-Rodiño is a research engineer and Ph.D. candidate at GTE research group (CINTECX, University of Vigo, Spain). He has his bachelor degree in mechanical engineering and his Master of Science degree in industrial engineering, both at University of Vigo. He completed his bachelor and master final projects in international companies. He has conducted research at Repsol Technology Lab on projects related to lubricant optimization for motorsport and commercial vehicles applications. Currently, his research focuses on studying hydrogen behaviour in burners and domestic boilers.

Martí Cortada-García works at Repsol Technology Lab, Spain, as a product design scientist. He is a chemical engineer and holds his Ph.D. degree in chemical engineering in the field of computational fluid dynamics. He is also a lecturer of CFD at the Autonomous University of Barcelona, Spain. He has publications in international journals in the fields of pyrolysis, process simulation, rheology, tribology, and lubrication.

Francisco J. Profito is an assistant professor of mechanical engineering at the Polytechnic School of the University of São Paulo, Brazil. He holds his M.Sc. and D.Sc. degrees in mechanical engineering from the same institution, specializing in the tribology of lubricated contacts. With three years of industry experience and research stays at Argonne National Laboratory, USA, and Imperial College London, UK, his research interests include computational tribology, bearings lubrication, and ML/AI applications in tribology. His work spans several engineering domains, including automotive engines, agricultural machinery, and wind turbines, focusing on improving system performance and durability across various industrial applications.

Jacobo Porteiro holds his Ph.D. degree and is an industrial engineer and full professor at the University of Vigo, Spain, in the field of thermal engines. He is the co-author of more than 130 journal papers and of more than 100 international conference papers. He has an h-index of 32 and more than 4,191 citations in Scopus. In 2014, he was appointed delegate for Spain at the Combustion Committee of the IEA, and later served as Chair of this Committee (2016–2017). He was Head of the Department of Mechanical Engineer from 2012 to 2018. He currently serves as Deputy to the Rector of the university for sustainability. His research focused on the modeling of combustion, heat and mass transfer in engineering applications, and with a recent work on the use of machine learning techniques to the acceleration of CFD models. He is the Member of the GTE Research Group that belongs to CINTECX (Research Centre in Technologies, Energy, and Industrial Processes).